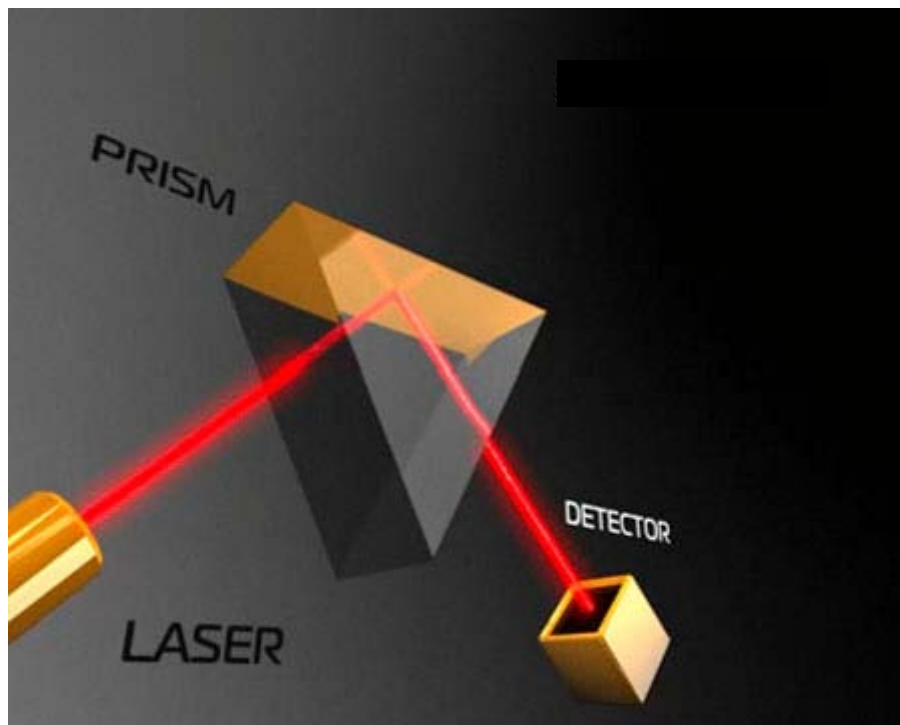


Exciting surface plasmons with a Mid-IR OPO

Bachelor assignment Applied Physics



Authors: *B.S. Ploeg*
K.W. Melis
Date: *10th of July, 2012*
University of Twente
Supervisors: *Prof. Dr. K.J. Boller*
MSc. J.P. Epping

Summary

Surface plasmon polaritons are commonly used in chemical and biological applications. The physical applications of surface plasmon polaritons are less common, but promises to be useful in nonlinear effects such as frequency doubling.

The propagation length of a surface plasmon polariton is low (typically 10 to 100 μm) due to absorption, radiation and coupling. The propagation length might be longer for long wavelengths. The goal of this experiment was to excite surface plasmon polaritons at thin films of metal in the Kretschmann configuration with a mid-infrared optical parametric oscillator.

The metals used are thin layers of aluminium, copper and gold in the range of 12 to 36 nm deposited onto a lithium niobate wafer. The wafer is attached to a gadolinium germanium garnet prism with the use of immersion oil. The excitation of a surface plasmon polariton is detected by measuring the angular reflectivity spectrum of the configuration.

The goal of this research is achieved, the determined propagation lengths (if only Ohmic losses are taken into account) are in the range of 20-200 μm , which can be concluded from measurements of the angular reflectivity curve and calculations based on Fresnel's equations.

Contents

1	Introduction.....	3
1.1	Introduction to SPPs.....	3
1.2	Problem statement.....	3
2	Theoretical aspects.....	4
2.1	Properties of SPPs	4
2.2	Excitation of SPPs	4
2.3	Detection of SPP's.....	6
2.4	Propagation length.....	7
2.5	Fresnel's equations.....	8
3	Experimental aspects	9
3.1	Method of research.....	9
3.2	Experimental setup	9
3.3	LabVIEW program.....	11
4	Results	12
4.1	Angular reflectivity spectrum of a 50 nm Gold film deposited onto a calcium fluoride prism 12	
4.2	Divergence of the beam	13
4.3	Measurements on the blank calcium fluoride prism	14
4.4	Excitation of SPPs with a 50 nm gold film deposited onto a calcium fluoride prism.....	15
4.5	The GGG prism	17
4.6	Lithium niobate attached to a GGG prism with a film of immersion oil	18
4.7	Metal films onto Lithium niobate, attached to a GGG prism with a film of immersion oil... 20	
5	Discussion.....	23
6	Conclusion	25
7	Appendices	26
7.1	Appendix A: Dispersion relation of a SPP	26
7.2	Appendix B: Drude model	29
7.3	Appendix C: Fresnel's equations [4].....	30
7.4	Appendix D: Angular reflectivity spectra of the samples	33
7.5	Appendix E: Measured thicknesses with a profilometer	35
8	Bibliography.....	37

1 Introduction

1.1 Introduction to SPPs

Surface plasmon polaritons (SPPs) are electromagnetic waves bound on the interface between a dielectric medium and a metal. These are used for detecting molecular absorption [1] or for example the detection of gas [2]. The waves consist of electromagnetic waves in the dielectric medium and electron oscillations in the metal (Figure 1.1a). Because of this combination SPPs can only propagate along the surface between these two media.

The fact that SPPs only propagate along the surface does not mean that the (electric) field inside the media is zero. In fact, the magnitude of these fields is exponentially decaying in the z -direction (Figure 1.1b).

Due to Ohmic losses, radiation and scattering the propagation length of a SPP is short (typically 10-100 μm [3], maximum propagation lengths are in the order of $\sim 1\text{mm}$ [4]). The research field of long range ($>100\ \mu\text{m}$) plasmons is young and strong excitation of SPPs with coherent mid-infrared sources is rare, especially with an OPO. Excitation of SPPs in lithium niobate (LiNbO_3) has not yet been achieved and achieving this excitation would be very important progress in the research field of plasmonics.

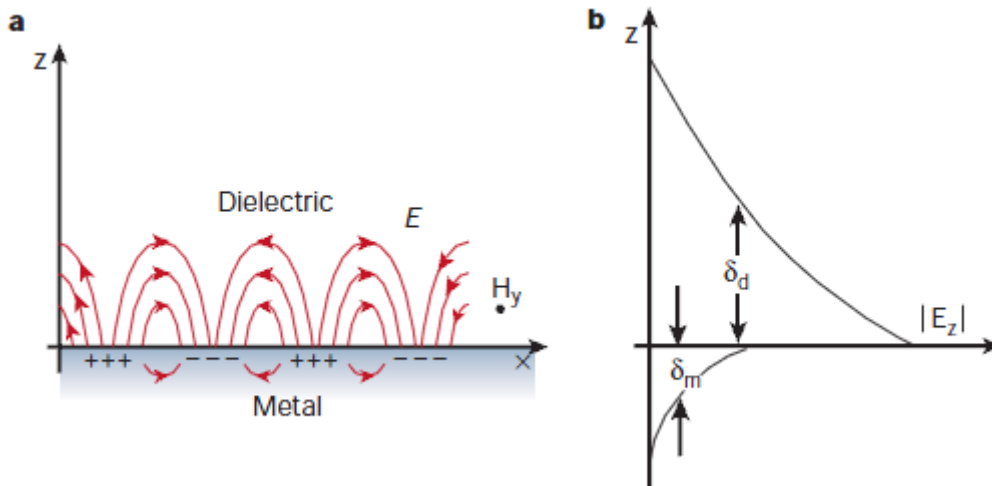


Figure 1.1a: Schematic view of a SPP propagating in the x direction at a metal/dielectric interface [3].

1.1b: The magnitude of the electric field in the z -direction.

1.2 Problem statement

The main goal of this research was to excite surface plasmon polaritons using a coherent mid-infrared light source. The project was divided into sub goals:

- Excitation of surface plasmon polaritons at a wavelength of 1064 nm in the so-called Kretschmann configuration with a calcium fluoride prism with a 50 nm layer of gold deposited onto it and with an aluminium layer deposited.
- Excitation and detection of surface plasmon polaritons with a Gadolinium Gallium Garnet (GGG) prism on films of different metals of various thicknesses deposited onto a lithium niobate substrate in the near and mid IR wavelengths of 1.064 μm and 2.33 μm respectively.

The motivation for the use of 2.33 μm is to excite surface plasmon polaritons with a long (more than 100 μm) propagation length.

2 Theoretical aspects

2.1 Properties of SPPs

A SPP is an electromagnetic wave as depicted in Figure 1.1a, and can thus be described by Maxwell's equations. As shown in Appendix A, the wave vector of the SPP depends on the dielectric constants of the materials used (ϵ_1 and ϵ_2) and the frequency (ω_{SPP}) of the wave:

$$k_{x,SPP}^2 = \left(\frac{\epsilon_1 \epsilon_2}{\epsilon_1 + \epsilon_2} \right) \frac{\omega_{SPP}^2}{c^2} \quad (2.1)$$

$$k_{z,SPP}^2 = \left(\frac{\epsilon_1^2}{\epsilon_1 + \epsilon_2} \right) \frac{\omega_{SPP}^2}{c^2} \quad \text{for } z < 0 \quad (2.2)$$

$$k_{z,SPP}^2 = \left(\frac{\epsilon_2^2}{\epsilon_1 + \epsilon_2} \right) \frac{\omega_{SPP}^2}{c^2} \quad \text{for } z > 0, \quad (2.3)$$

where c is the speed of light, x is the propagation direction along the interface, z is pointed perpendicular to the interface as shown in Figure 2.1.

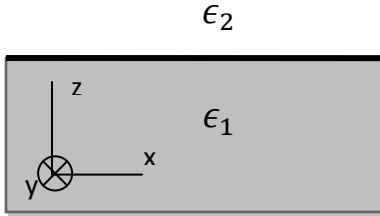


Figure 2.1: Interface between material 1 with the dielectric constant ϵ_1 and material 2 with ϵ_2 .

Looking at equations 2.1-2.3 in order to obtain propagation in the x direction ($\Re(k_{x,SPP}) > 0$) but not in the z direction ($\Re(k_{z,SPP}) = 0$), two additive conditions can be set:

$$\Re(\epsilon_1 \cdot \epsilon_2) < 0 \quad (2.4)$$

and

$$\Re(\epsilon_1 + \epsilon_2) < 0. \quad (2.5)$$

The only combination of two media capable of fulfilling these two conditions is a combination of a complex valued ϵ_1 with a negative real part, such as a metal, and a positive real valued and frequency independent ϵ_2 , such as a dielectric material.

2.2 Excitation of SPPs

In order to excite surface plasmon polaritons both the value of the wave vector and the frequency of the SPP and the incoming wave have to be the same, which is called phase matching. What we want to derive is the point at which phase matching takes place. The two dispersion relations, of the SPP and the light in the dielectric intersect and energy transfer between the incoming wave and the SPP is most efficient (SPP resonance).

The dielectric constant of a metal can be approached by the Drude model (see Appendix B):

$$\epsilon_1(\omega_{SPP}) = 1 - \frac{\omega_p^2 \tau^2}{1 + \omega_{SPP}^2 \tau^2} \quad (2.6)$$

where τ is the relaxation time of the free electron gas and ω_p is the plasma frequency.

Combining equations 2.1 and 2.6 gives the dispersion relation of a SPP. In Figure 2.2, both dispersion relations are plotted.

The wave vector of the dielectric (k_d) is given a:

$$k_d = \sqrt{\epsilon_2} \cdot \frac{\omega}{c}, \quad (2.7)$$

where ϵ_2 is the (real) dielectric constant of the dielectric material.

In the following example a SPP will be excited in the Kretschmann configuration with a prism of glass, a metal layer on top of it in air. ϵ_2 in this example is air and ϵ_1 is the dielectric constant of the metal.

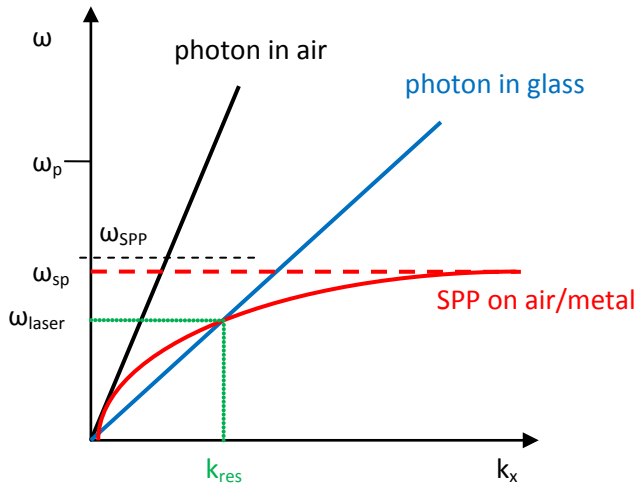


Figure 2.2: Dispersion relation of SPP waves propagating at the air/metal interface [3].

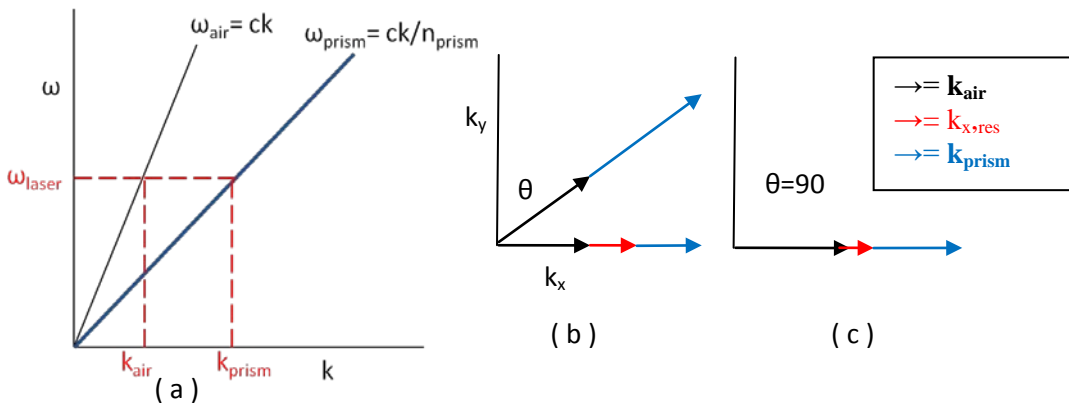


Figure 2.3a: Dispersion of light in air and in glass. b: Components of the k vector in air, glass and resonant k_x vector. c: The maximum magnitude of the k_x vectors.

In Figure 2.2 the linear solid lines are the dispersion relations for light in air and glass respectively. The nonlinear curve depicts the dispersion for a SPP (according to the Drude model) at an air/metal interface (2.6 and 2.1 combined). ω_p is the plasma frequency of the metal and is a constant. The dashed horizontal red line is asymptotic value ω_{sp} which the SPP curve will reach for large k_x vectors.

$$\lim_{k_x \rightarrow \infty} \omega_{sp} = \frac{\omega_p}{\sqrt{1 + \epsilon_2}}. \quad (2.8)$$

The SPP is excited by energy and momentum matching (phase matching) between the incident electromagnetic wave in glass and the electron density oscillators in the metal. ω_{laser} is the frequency

of the incident light in air. If there is only an air/metal interface such as in Figure 2.4a then the phase matching condition cannot be fulfilled. The reason is that the SPP curve cannot intersect the dispersion curve of light in air because the magnitude of the k_{air} vector of light in air is constant and lower than the k_{res} vector needed for SPP excitation, compare the size of the black vector in Figure 2.3c with the red. The dispersion relation of light in air in Figure 2.2 cannot intersect the SPP air curve because of this. They only intersect at $k_x=0$ where there is no solution for a wave at all.

If we add a layer of glass in the form of a prism like in Figure 2.4b then the k vector in glass will be larger than the k vector of light in air, see Figure 2.3a. Because the size of the k vector in this configuration becomes k_{prism} and can be made larger than k_{air} by choosing an appropriate high index for the prism, material resonance can be provided. The slope of the dispersion relation of glass can be varied by changing the angle of incidence until it intersects with the SPP air curve at the point ω_{laser} and achieve phase matching.

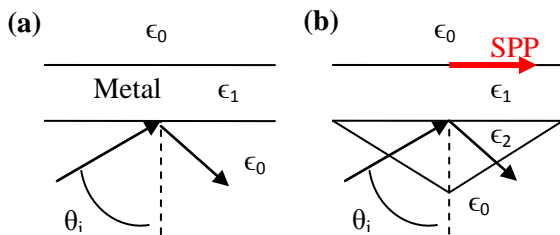


Figure 2.4a: A metal sandwiched in air. b: Air, metal, glass layer

There are several more ways to match the wave vectors, for example by using a grating. The two principles making use of a prism made out of a third medium are the Kretschmann- and the Otto configuration (Figure 2.5a and 2.5b), [5]. The Otto configuration makes use of an air layer between the metal and the coupling prism. An evanescent wave is generated at the air/prism interface. This wave will bridge the air gap and reach the metal layer where it can excite a SPP. In the Kretschmann configuration the gap is made out of metal and a SPP will still be excited at the air/metal interface. In our experiment the Kretschmann configuration was chosen because of the practical difficulties of providing an air gap with reproducible thickness in the Otto configuration.

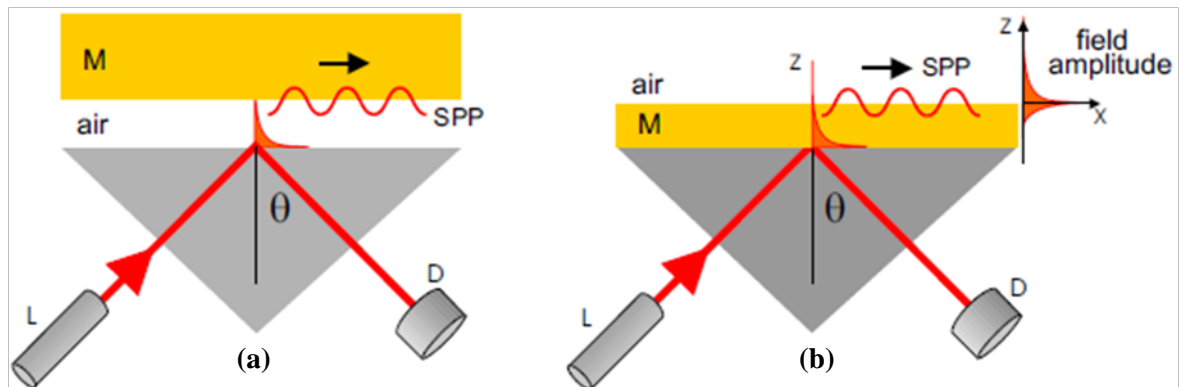


Figure 2.5a: Otto Configuration. b: Kretschmann configuration. L=laser, D=detector, M=metal layer. [2]

2.3 Detection of SPP's

The detection of SPP's can be done in several ways. The fact that a light wave can couple to a SPP does on one hand mean that SPP's can be excited by the incident light under a certain angle θ . On the other hand however, it also means that SPPs can couple light back into the prism. This emitted light can be detected. Also scattering losses due to impurities at the interface will cause the SPP to emit light, though at different angles than θ which might be detected as well.

Another way of detecting SPPs is by using an Atomic Force Microscope (AFM) positioned near the surface where the SPP should be excited, with which the electric field can be detected.

In our experiment, the reflected light has been detected in dependence of the angle of incidence in the Kretschmann configuration. For angles larger than the angle of total internal reflection, the light is completely reflected unless the light couples to a SPP. The excitation of a SPP results in a lower intensity of the reflected beam.

2.4 Propagation length

As a SPP propagates along the surface, it loses energy to the metal due to absorption, scattering by impurities and radiation back to the coupling prism. The propagation length is defined as the distance for the SPP intensity to decay by a factor of $1/e$.

A deeper dip in the reflectivity against angle of incidence means that more power can be transferred to the SPP, but the higher power does not affect the propagation length.

Typically the propagation losses of a SPP are high, resulting in low propagation lengths of order 10 to 100 μm . The absorption is described by the imaginary part of the dielectric constants of the metal used. The propagation length of the SPP due to absorption ($\delta_{SPP,a}$) can be derived in the following way [6]:

$$\delta_{SPP,a} \equiv \frac{1}{2 \cdot \Im(k_{SPP})} = \frac{c}{\omega} \cdot \left(\frac{\Re(\epsilon_m) + \epsilon_d}{\Re(\epsilon_m) \cdot \epsilon_d} \right)^{\frac{3}{2}} \cdot \frac{\Re(\epsilon_m)^2}{\Im(\epsilon_m)} \quad (2.9)$$

with the assumption that the dielectric is loss free ($\Im(\epsilon_d)=0$).

An indication for the propagation length due to the radiation back into the coupling prism is the angular width of the dip in the reflection curve, a wider dip means that resonance also occurs at angles slightly different than the resonance angle. The result is not only that SPP's can be excited at these angles, but also that radiation back into the prism takes place at more angles.

2.5 Fresnel's equations

In order to determine the propagation length (due to Ohmic losses) of the SPPs (equation 2.9), the dielectric constant of the metal and of the dielectric medium have to be determined. One way to calculate these is by use of the Fresnel's equations. The reflectivity of a configuration of multiple layers can be calculated with the Fresnel's equations, described in Appendix C. An example of the calculated reflectivity versus the angle of incidence is shown in Figure 2.6 for the specific case of a 50 nm gold layer deposited on a calcium fluoride prism.

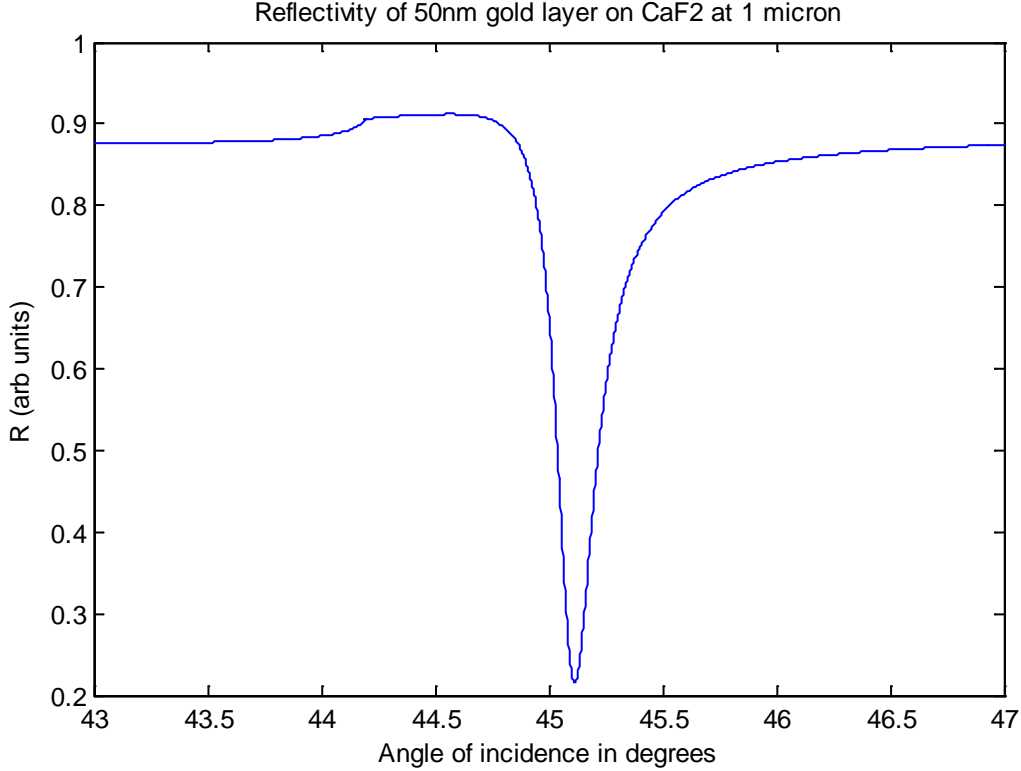


Figure 2.6: The angular reflectivity spectrum of a 50 nm thick layer of gold deposited onto a calcium fluoride prism. On the horizontal axis is the angle of incidence with respect to the metal surface, the vertical axis gives the reflectivity.

It can be seen that at an angle of approximately 45.2 degrees a minimum in the reflectivity occurs. In comparison to this SPP resonance should theoretically occur at an angle (θ_{Res}) where the x-component of the dispersion relation of the calcium fluoride prism and the dispersion relation of the SPP match:

$$\epsilon_{CaF2} \cdot \sin(\theta_{Res})^2 = \left(\frac{\epsilon_1 \epsilon_2}{\epsilon_1 + \epsilon_2} \right). \quad (2.10)$$

In this formula, ϵ_{CaF2} is the dielectric constant of the prism, θ_{Res} is the angle of resonance and ϵ_1 and ϵ_2 are the dielectric constants of gold and vacuum.

The solution of equation (2.10) predicts the generation of a SPP at an angle of incidence of $\theta_{res} = 45.167$ degrees. This value is, the errors in precision of the dielectric constants used taken into account, in agreement with the angle where the dip was observed in the Fresnel calculations (Figure 2.6).

Secondly, Figure 2.6 shows a discontinuity at an angle of incidence of 44.17 degrees. This corresponds to the angle of onset of total internal reflection. In a simple configuration of two layers, the reflectivity of the system should be equal to one for angles larger than the angle of total internal reflection. In this case however, the incoming wave loses energy due to Ohmic losses in the metal, causing the reflectivity to be somewhat lower.

3 Experimental aspects

3.1 Method of research

In this experiment, a SPP can propagate along the surface between a metal (silver, gold or copper) and air. The metal is deposited onto a lithium niobate substrate, which can be put onto a Gadolinium Gallium Garnet (GGG) prism or a calcium fluoride (CaF_2) prism. The SPP will be excited by a laser with a wavelength around $1 \mu\text{m}$ and by an optical parametric oscillator (OPO) around $2.3 \mu\text{m}$.

The SPP can be detected by a dip in the angular reflectivity spectrum. The angle of the minimum of the dip is larger than the critical angle of total internal reflection and characterises the maximum resonance.

The minimum of the dip corresponds to a maximum of the SPP resonance, which will only occur under a certain angle. At maximum resonance the photons couple strongest to the electron oscillations. To find this angle experimentally, the angle of incidence, between the beam and the normal of the metal surface is systematically varied while the intensity of the reflected beam is recorded with a photodetector.

If the excitation wavelength increases, the losses in the metal will decrease (see equation 2.9). This results in a longer propagation length and is the reason why, in this research, we aim to generate a SPP with a mid-IR excitation wavelength. Propagation lengths had to be calculated before a choice of possibly suitable metals could be made which have high propagation lengths.

3.2 Experimental setup

Three different metals (gold, copper and aluminium) were each deposited onto a lithium niobate substrate. The choice of metals is based on the calculated propagation lengths (for Ohmic losses only taken into account) with the aid of formula (2.9). The calculated values are 1.76 mm for aluminium, 1.22 mm for gold and 0.84 mm for copper. These values were calculated for a wavelength of 1064 nm. There are metals with higher propagation lengths than copper (such as molybdenum and silver), but the choice for copper was based on the fact that the material is not widely used for plasmonic experiments and might lead to interesting results.

The substrates used in these experiments were made of lithium niobate. As the refractive index of lithium niobate is relatively high (around $n=2.2$ at a wavelength of 2330 nm), and to avoid having to use lithium niobate in the form of prisms, the decision has been made to accomplish input coupling with a prism of Gadolinium Gallium Garnet (GGG). The GGG prism has a relatively high refractive index ($n=1.94$ at 1064nm and $n=1.925$ at 2330nm [7]) and therefore allows a big range of k_x values compared to fused silica glass or other common coupling materials. The metal coated substrate is attached to the prism by immersion oil (with unknown refractive index). The oil has been used to lower the index step at the GGG/lithium niobate interface.

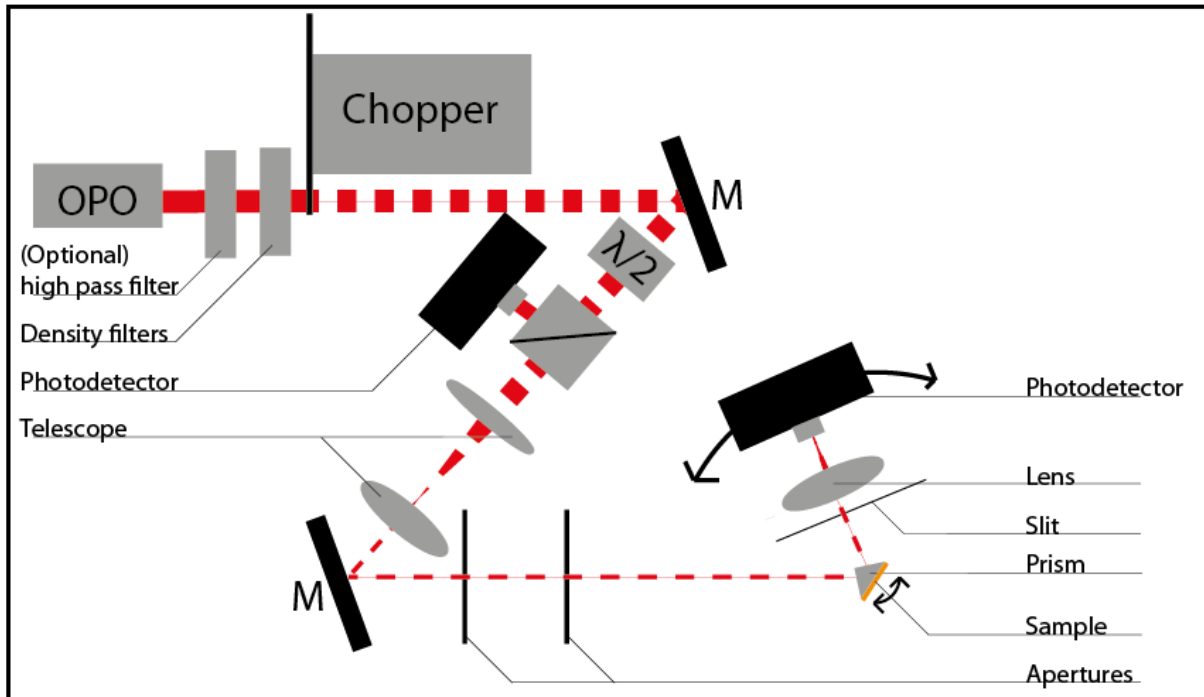


Figure 3.1: Schematic representation of the experimental setup.

The setup used to measure the reflection curve of a certain layer mounted on the prism is displayed in Figure 3.2. The laser used was an Ytterbium fibre amplified diode laser at a wavelength of 1040 nm. An optical parametric oscillator (OPO) could be used to generate laser light of 2330 nm. An optional high-pass filter in combination with this OPO made it possible to switch between the two wavelengths.

After the long-pass filter, reflective filters were placed to decrease the intensity of the beam. Together with a chopper to create pulses this was found necessary to avoid saturation of the photodetectors.

Due to power fluctuations of the OPO of about 20% in less than a second, measurements on the intensity of the incoming beam had to be done as a reference. For this purpose a part of the laser beam was reflected to photodetector 1 using a polarizing beam splitter (PBS) and a half-wave plate. The PBS splits the light into two transverse polarization components, while the ratio of the intensities of these could be set with the half wave plate. SPPs are p-polarized, which means that the electric field is pointing in the plane of incidence and the magnetic field perpendicular to this plane (as described in Appendix A). Therefore SPPs can only be excited with p-polarized light. In order to give the best measurable dip in the angular reflectivity spectrum the s-polarized light must be filtered out. This has been done by adjusting the half-wave plate.

Divergence would broaden the width of the dip in the angular reflectivity spectrum. With use of the telescope the divergence of the beam at the prism surface has been minimized. As a side aspect, the telescope reduced the size of the beam, maximizing the part of the beam that couples into the prism.

The prism was placed coincident with the rotational axis of a rotational stage (Thorlabs CR1-Z7), with which the angle of incidence could be varied. The reflected beam was detected with a photodetector (Thorlabs PDA30G) beyond a lens ($f=25$ mm), mounted onto a second rotational stage (Thorlabs CR1-Z7) coaxial with the first rotational stage. The surface of the prism and both rotational stages are coaxial with an estimated error of 2 mm.

Both the rotational stage of the prism and the rotational stage of the detector were motorized and controlled by LabVIEW. The automatic recording increased the overall recording speed significantly at high angular resolution. A maximum recording speed is of importance in view of drift in experimental performance, such as the output parameters of the radiation of the OPO.

3.3 LabVIEW program

The LabVIEW program used to measure the angular reflectivity spectra controlled the two rotational stages and measured the voltages of the two photo detectors using a LabVIEW data acquisition set.

The angle of the prism to the incoming beam had to be calibrated before recordings could be done. At an angle of incidence of 45 degrees, the laser beam hits the surface of the prism at an angle of 90 degrees to the surface of the prism. A part of the light was reflected and this beam then overlapped with the incoming beam.

The detector stage turned out to be moving at random moments due to an error in the driver software. The calibration had then to be done again, which implies that also the prism had to be calibrated again. Calibration of the detector stage by removing the prism from the stage turned out to lead to errors in the position of the prism. This was avoided with calibration by setting the prism at a certain angle, with which the angle of the reflected beam to the incoming beam could be determined as to two times the angle of incidence. The program started with scanning a range of angles around the manually found value while measuring the intensity of the beam and the angle at which maximum power occurred was then taken as the angle of the detector.

After this calibration the angle of incidence could be set as described, and the detector arm was set at twice the angle of incidence (which from now on will be called the calculated angle of the beam). In order to make sure the prism and the detector stages were at the right angles, the positions of the stages were compared to the positions they should have. If they did not agree the stages were moved again, and this procedure was repeated until the stages had the right angle with an error of 0.01 degrees. The LabVIEW data acquisition set then measures both the voltage output of the photodetector placed at the incoming beam (as a reference) and the voltage output of the photodetector placed at the reflected beam.

Besides the need of the chopper to avoid the photodetectors from saturation, the intensity measured with the photodetectors was more accurate due to the (approximately) square wave of power versus time. The amplitude of this wave was assumed to be proportional to the power of the laser beam. The minimum value of the power is higher than zero due to background light, whereas the maximum value of the power is the power of the beam plus the background light. By taking the amplitude of the square power wave only the power of the beam was taken into account.

The fluctuations in the power of the incoming beam (due to fluctuations in the OPO) had a strong influence on the measured intensities. However it was observed that these fluctuations occur at (random) time-intervals, with time-intervals of little fluctuations of power in between. In order to find such intervals of little fluctuations the intensity of the beams was measured five times in a time span of 0.5 seconds. Only if the five measurements of the power of the incoming wave were the same within a range of 5 percent of the mean intensity the mean value of the measured ratios between the reflected beam and the incoming beam was taken to be the ratio of intensities.

Due to the use of filters, lenses and other optical elements the measured ratio of power was proportional to the reflectivity coefficient. Because of this, the recorded angular reflectivity curves were normalized to fit for example calculated angular reflectivity curves.

4 Results

4.1 Angular reflectivity spectrum of a 50 nm Gold film deposited onto a calcium fluoride prism

In order to measure the angular reflectivity spectrum of this configuration the angle of incidence was set with a rotational stage. With a power meter (Newport 841-PE) the power of the reflected beam was measured. As indicated in Figure 4.1 the angle of incidence is defined as the angle of the incoming beam in air to the normal of the sample.

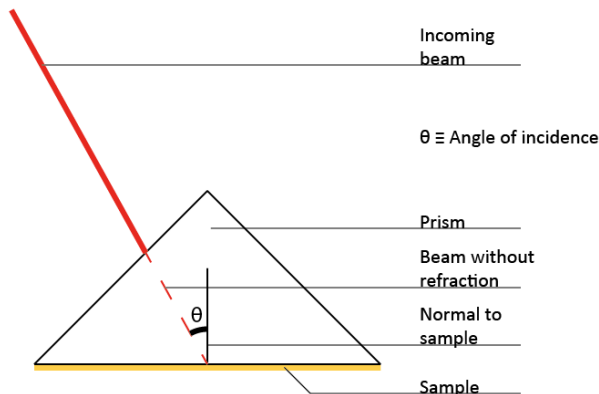


Figure 4.1: Definition of angle of incidence.

With the refractive indices ($n=1.30824$ for calcium fluoride, $n=1$ for air and $n=0.27668+7.1706*i$ for gold) [8]) and Fresnel's equations the angular reflectivity spectrum has been calculated. In Figure 4.2 both the measured reflectivity (blue) and the calculated angular reflectivity spectrum (green) are displayed.

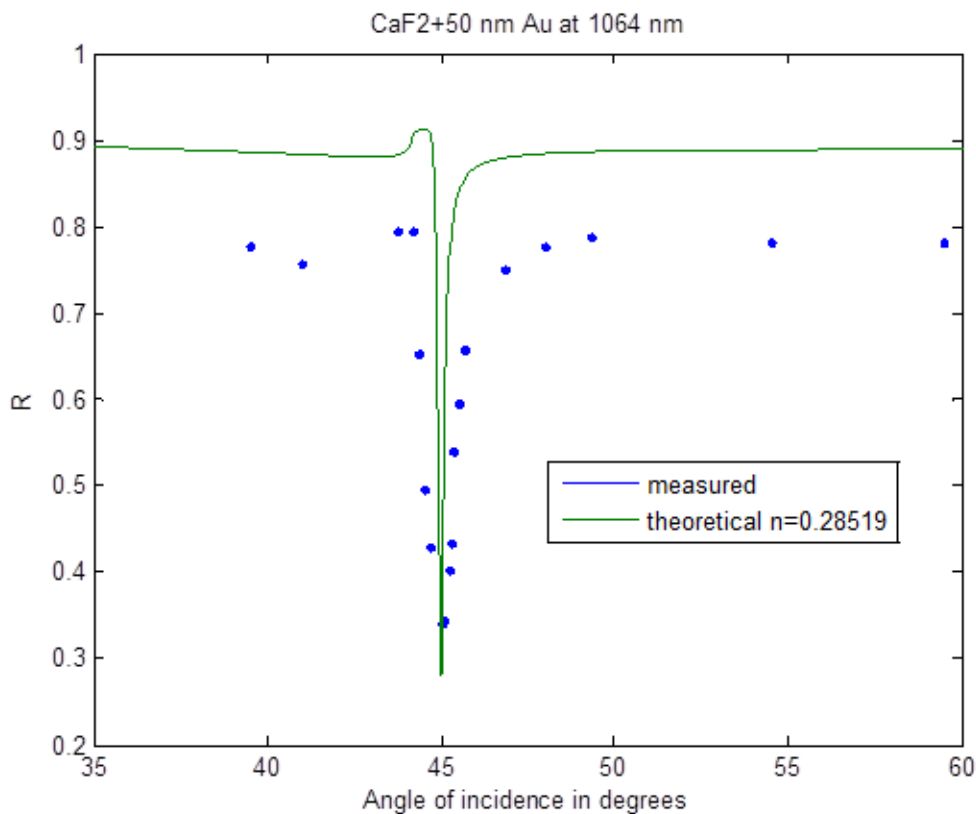


Figure 4.2: The theoretical and measured angular reflectivity spectrum of a 50 nm thick layer of gold deposited onto a calcium fluoride prism. The incoming laser beam had a wavelength of 1064 nm.

As can be seen, the location of the dip in the calculated angular reflectivity spectrum is located at the angle where a dip in the measured angular reflectivity spectrum has been observed. However the measured reflectivity is systematically lower than the theoretical values. This is assigned to the fact that the theoretical curve does not take all losses into account, such as scattering due to the finite surface roughness of the involved surfaces.

At an angle of approximately 45 degrees a minimum occurred in the reflectivity. This strongly indicated SPP resonance and thus the excitation of a SPP. The conclusion that can be drawn from this result is that SPP resonance can be achieved with this setup.

The theoretically expected value of the width of the dip in the angular reflectivity spectrum is smaller at a wavelength of 2330 nm than the width of the dip at 1064 nm. Finding and measuring this dip requires a higher angular resolution than in Figure 4.2

4.2 Divergence of the beam

At higher angular resolution, it turned out to be of importance to investigate effects such as the divergence of the beam. The incoming beam has a certain divergence, which results in a range of angles of incidence at the surface of the metal sample. With the manual recordings the whole beam (or at least 90% of the intensity) was detected due to the relatively large area of the detector (113 mm²). Every data point in Figure 4.2 does therefore not correspond to one angle, but to a range of angles.

For the automated recordings, a Thorlabs PDA30G photodetector with a width and height of 3 mm was used to process the recorded data automatically. A slit (with a maximum width of 0.25 mm) was placed between the prism and the detector at a distance of 51 mm to the rotational axis of the stages in order to decrease the range of measured angles of incidence for each measurement to 0.005 degrees. With this slit in front of the detector the power of the beam at a wavelength of 2330 nm versus the angle of incidence has been measured (Figure 4.3). The power has been normalised to the maximum power of the beam.

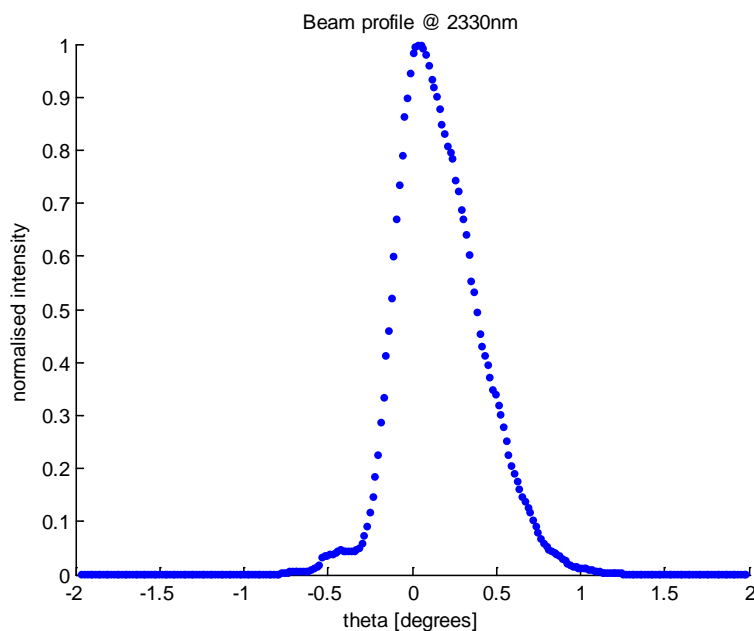


Figure 4.3: The power of the beam as function of the angle of incidence (*theta*).

As can be deduced from Figure 4.3 the beam profile has a half-power beamwidth of 0.508 degrees (relative to the angle axis of the rotational stage). This value is more than 100 times the range of angles measured for each data point, the range of angles measured at each position of the detector is thus dependent of the size of the slit rather than on the divergence of the beam.

A second conclusion which can be deduced from the beam profile in figure 4.3 is the importance of measuring the power of the reflected beam at the right angle. An error in the position of the detector of for example 0.234 degrees would have caused an error in the measured intensity of 50 percent relative to the maximum value of the intensity.

4.3 Measurements on the blank calcium fluoride prism

Our setup, described in Paragraph 3.2, measures the intensity of the beam at twice the angle of incidence to the normal of the metal surface with regard to the rotation axis of the rotational stage (from now on this method will be referred to as the fast method).

This method of recording turned out to cause some problems. Due to refractions in the prism and alignment errors, the reflected beam did not always propagate from the middle of the rotational stages, as is shown in Figure 4.4.

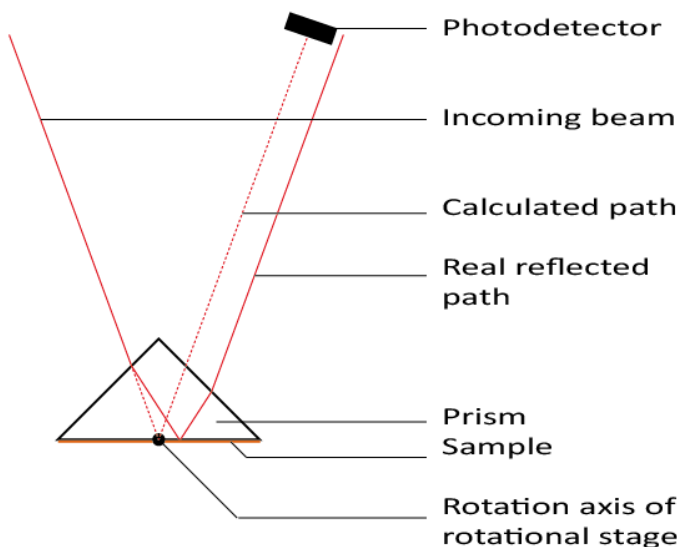


Figure 4.4: Mismatch of the measured beam.

As it turned out, this mismatch has been the cause of systematic errors in the angular reflectivity spectra recorded in further experiments. The power profile of the reflected beam formed a Gaussian distribution with the maximum value at the real reflected beam (as defined in Figure 4.4) Due to the mismatch, the measured intensity with the photodetector placed at the calculated path was lower than the maximum value. This mismatch will be higher for angles of incidence further away from the angle of incidence at which the detector has been calibrated. The fast method thus gives a lower reflectivity at angles further away from to the angle of incidence at which the detector has been calibrated.

With the automated setup, a second way to measure the angular reflectivity spectrum was done by setting a certain angle of incidence and then scan a range of angles around the predicted angle. The resulting data points form the angular power profile of the reflected beam at this specific angle of incidence. With this profile the maximum power of the reflected beam was calculated. This procedure was repeated for different angles of incidence, and the angular reflectivity spectrum was then plotted. This method of recording data will be referred to as the slow method.

Although the slow method was more precise in measuring the reflectivity at a certain angle of incidence, the fast method was preferred because of random fluctuations in the radiation parameters of the OPO. To decide which method to use in further experiments, the results of both methods were compared. The angular reflectivity spectra obtained with both methods are plotted in Figure 4.5.

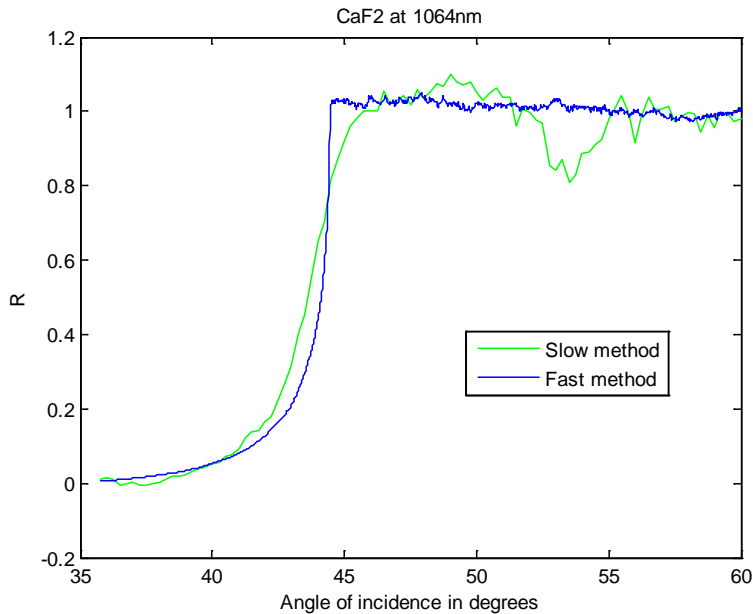


Figure 4.5: Angular reflectivity spectra recorded with the slow and the fast method, using as sample the surface of a blank calcium fluoride prism at a wavelength of 1064 nm.

It can be seen that the angular reflectivity spectrum measured with the fast method shows the same curve as measured with the slow method within a range of reflectivity of 0.2. Besides this, the curve measured with the fast method shows nearly no deviation from one at higher angles whereas the measured angular reflectivity curve obtained with the slow method does show fluctuations of about 0.2.

The recorded data with the slow method should have shown fewer fluctuations than the fast method. The cause of these fluctuations was ascribed to a not-Gaussian beam profile. In order to measure the amplitude of the reflected beam, a Gaussian distribution was fitted to the measured angular power profile of the reflected beam. The amplitude of this Gaussian distribution was taken as the power of the reflected beam. A not-Gaussian power distribution of the reflected beam can have led to a big error in the calculated reflectivity curve.

Taking all this into account, the fast method has been chosen to measure the angular reflectivity spectra of the following samples.

4.4 Excitation of SPPs with a 50 nm gold film deposited onto a calcium fluoride prism

The angular reflectivity spectrum of the calcium fluoride prism with a 50 nm thick gold film used in the first experiment which is measured manually could now be measured automatically with a higher resolution. Still the wavelength used was 1064 nm, and therefore the angle at which SPP resonance was calculated was the same (around 45 degrees).

In Figure 4.7 the measured curve is plotted together with the same theoretical curve as used in Figure 4.2.

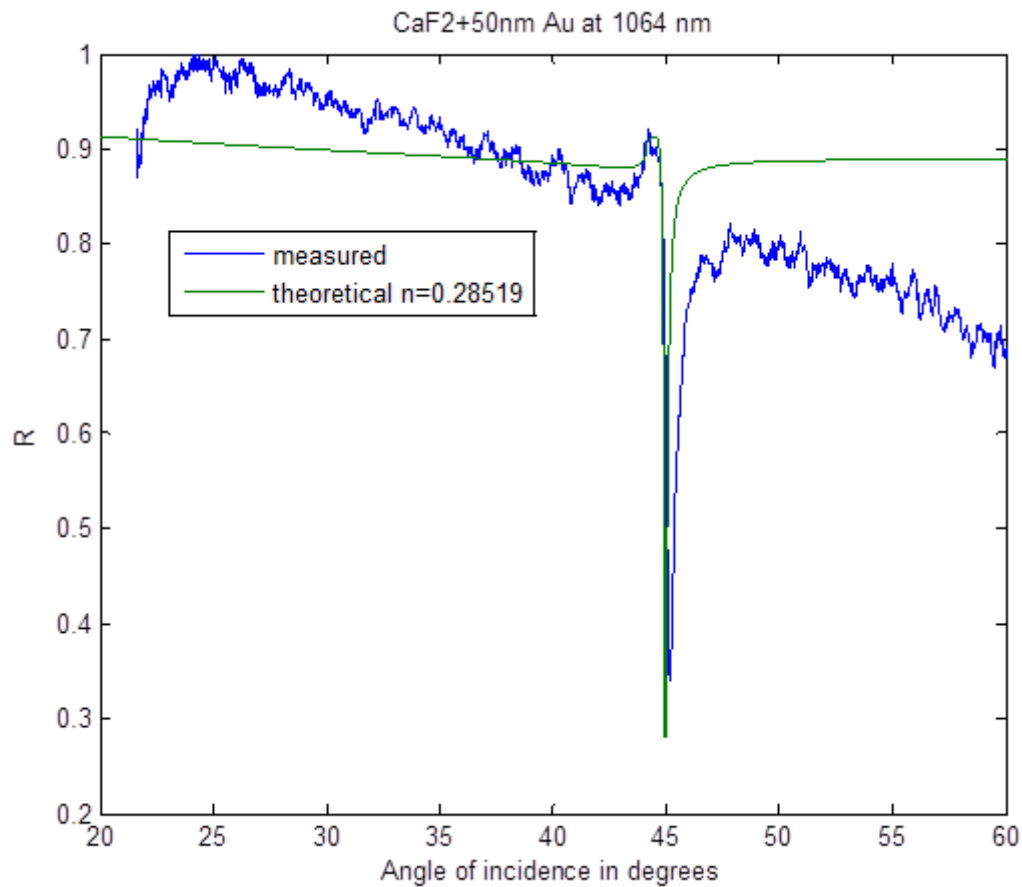


Figure 4.7: Theoretical and measured angular reflectivity spectra of a 50 nm gold film deposited onto a calcium fluoride prism at a wavelength of 1064 nm with the automated setup.

As can be seen the position and the depth of the dip fits the theoretical curve rather well. However, the measured curve shows an overall decaying function. If Figure 4.7 is compared with the same measurement for the slow method then the slow method shows no decaying. This is clearly a disadvantage of the fast method. However, the decaying function does not influence the angle at which SPP excitation occurs, and still the general shape of the dip can be observed.

4.5 The GGG prism

In order to compare later results with theoretical values, first the material properties of the prism, oil, lithium niobate and various metals have to be determined. The measurements in this paragraph were done with the Ytterbium-fibre pump laser in combination with the OPO, in order to measure with a near infrared wavelength of 1040 nm as well as with a mid-infrared wavelength at 2330 nm.

In this paragraph the refractive index of GGG is determined for the two named wavelengths. The refractive index of GGG can be calculated from a measurement of the critical angle. This angle has been observed by measuring the angular reflectivity spectrum of the GGG prism.

The first thing that is being plotted Figure 4.8 and 4.9 is the measured angular reflectivity spectra, as shown in blue in. The second step is to use the Fresnel equations together with the refractive index values from literature to calculate and plot the green coloured theoretical curve. The refractive index of GGG at these wavelengths [7] is 1.945 at 1040 nm and 1.925 at 2330 nm. In red are the angular reflectivity spectra plotted which give the best fit to the experimental data by adjusting the refractive index as parameter. A theoretical curve with refractive index of the GGG of 1.9484 at 1040 nm and 1.928 at 2330 nm fit the data best.

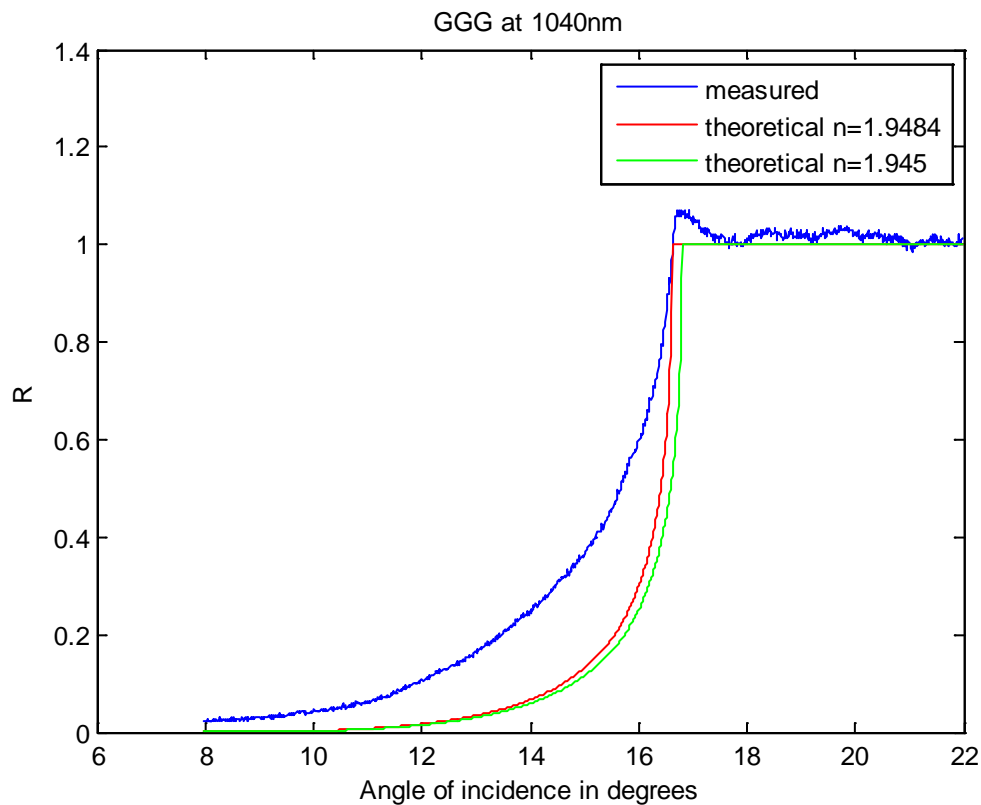


Figure 4.8: Angular reflectivity spectrum of the GGG prism at a wavelength of 1040 nm

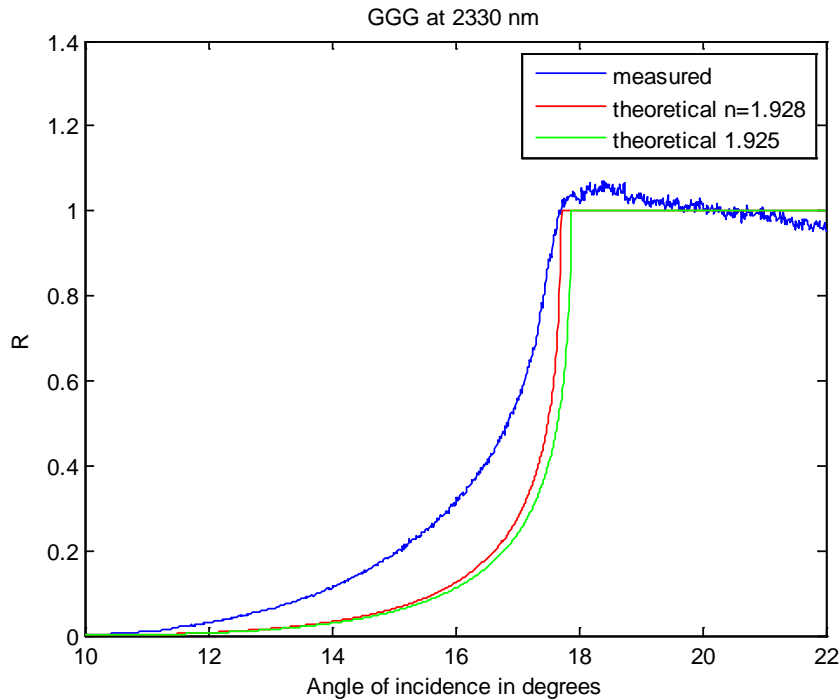


Figure 4.9: Angular reflectivity spectrum of the GGG prism at a wavelength of 2330 nm

As can be seen in both figures, the critical angles for total internal reflection of the GGG prism at both wavelengths match the theoretical critical angles determined with values found in literature in a range of 0.5 degrees.

The two values for the refractive index of the GGG from the fitted (red) curve will be used in further analysis.

Comparing the measured and the theoretical curves, the measured reflectivity for angles lower than the critical angle for total internal reflection was higher than the theoretical reflectivity predicts. It could be possible that the measured intensity was indeed higher than the theoretical reflectivity at these angles, but it could also have been that the measured reflectivity at higher angles was lower than the theoretical curve at points above the critical angle. This would then influence the normalization, resulting in the displayed changes of the slopes between the curves.

4.6 Lithium niobate attached to a GGG prism with a film of immersion oil

For the main experiments, various different metal films were deposited onto a lithium niobate wafer. The wafer was then attached to the GGG prism using immersion oil. In order to investigate the influence of the attachment of these two layers, namely the lithium niobate and the oil layer, the angular reflectivity spectrum of this system; the GGG prism attached to a layer of oil of unknown thickness followed by a layer of 0.2 mm lithium niobate has been measured. In Figures 4.10 and 4.11, the measured and the theoretical angular reflectivity spectra of this system are given for a wavelength of 1040 nm and 2330 nm. What is peculiar is that the measured curves show ripples in the angular reflectivity spectrum.

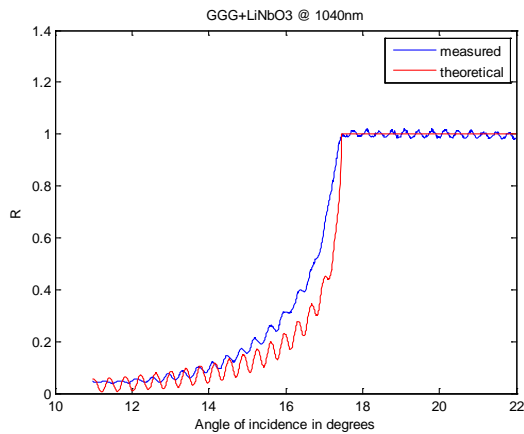


Figure 4.10: Angular reflectivity spectrum of the system GGG-oil-LiNbO₃ at a wavelength of 1040 nm.

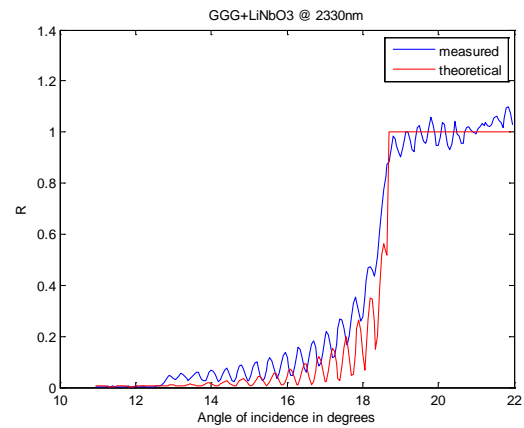


Figure 4.11: Angular reflectivity spectrum of the system GGG-oil-LiNbO₃ at a wavelength of 2330 nm.

The ripples in the angular reflectivity spectrum were caused by interference of the reflected waves inside the thin layer of oil and the layer of lithium niobate. In order to determine what caused the ripples a theoretical curve was modelled in which the thickness and refractive index of the lithium niobate and oil were used as a parameter.

Neither the refractive index nor the thickness of the layer of oil was determined, and the theoretical curves shown in Figures 4.10 and 4.11 were calculated using a refractive index of 1.5, which is typical of immersion oils [9]. The thickness of the layers was chosen to fit the data.

The influences of the refractive index and the thickness of the lithium niobate are small compared to the influence of the immersion oil. The period of the ripples caused by the lithium niobate was approximately 5 times as long as the period of the ripples due to the oil film. The amplitude of the ripples caused by the lithium niobate was less than half the amplitude of the ripples caused by the immersion oil.

After the measurement the thickness of the layer of oil could be calculated to 0.054 mm in the setup for the wavelength of 1040 nm and 0.032 mm for 2330 nm. This difference in thickness between the 1040 nm and 2330 nm measurement are due to a change of the amount of oil used for the two measurements.

For angles higher than the critical angle all light should reflect back, and the ripples should not be present. The fact that in these measurements the ripples are still present above the critical angle means that not all the light was reflected. This could be caused by s-polarized light present in the incoming beam. Even though a beam splitter in combination with a half wave plate has been used, s-polarized light could still be present, and could interfere in the oil-layer.

The thickness of the oil film changed every measurement. For a full modelling of the measurements in systems containing more layers, all parameters would have to be found. The layers of oil and lithium niobate only cause ripples with reflectivity changes small comparable to the change in the reflectivity due to SPP resonance (approximately 20 percent of the depth of the dip). In the experiments with a metal film deposited onto a LiNbO₃ wafer the measured curve was fitted by the theoretical curve of a system of GGG, metal and air, hereby ignoring interference in the oil film.

4.7 Metal films onto Lithium niobate, attached to a GGG prism with a film of immersion oil

In Figure 4.12 two curves are plotted. The blue curve gives the measured ratio between the intensity of the incoming laser beam and the intensity of the reflected beam from a configuration GGG-oil-lithium niobate-aluminium-air. This curve was normalized in order to fit the calculated curve.

The red curve gives the calculated reflectivity of the configuration GGG-aluminium-air. The following parameters have been used to calculate the red curve: a thickness of 12.9 nm of the aluminium layer was measured with a profilometer (see Appendix E), the refractive index of the prism has been determined in the previous paragraphs ($n = 1.945$) and the refractive index of the aluminium was found in literature ($\tilde{n} = 1.39438 + 9.9727 \cdot i$) [10].

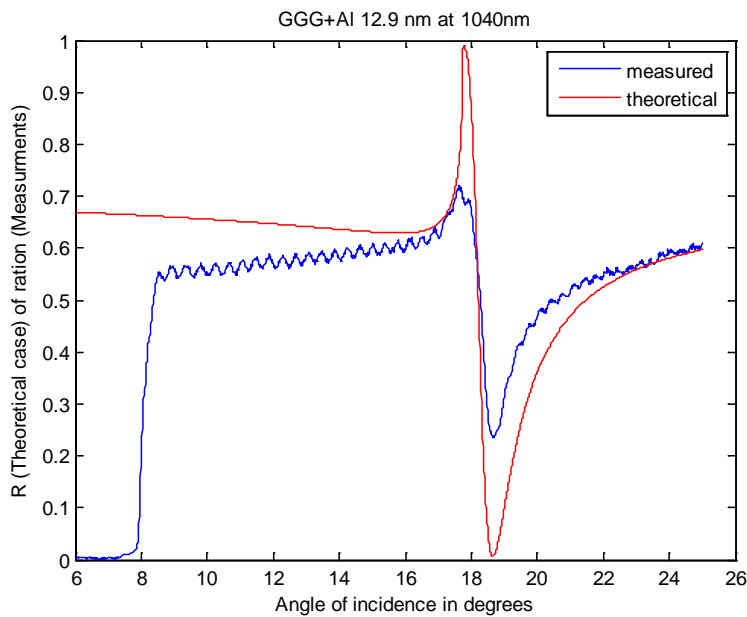


Figure 4.3: Theoretical curve (red) and measured ratio between the photo detectors (blue).

As can be seen in Figure 4.12 the angle of maximum SPP resonance is the same for the model as for the measured ratio. However, there are some differences. First the measured data is zero for angles lower than approximately 8 degrees. We found that this is because the detector blocked the incoming beam for these small angles. Secondly, the measured curve shows an increasing trend for angles in the range 9-16 degrees. We address this to the mismatch in the angle of the detector for the calculated position of the beam and the angle corresponding to the real position of the maximum of the beam.

Then, at angles around the SPP resonance, the amplitude of the measured dip is lower than the dip in the calculated angular reflectivity spectrum. As a possible explanation the calculations have been based on the ideal case of a perfectly p-polarized plane wave. In the experiment, the beam might have been partly s-polarized, causing a higher reflectivity at all angles of incidence (whereas the theoretical curve does only account p-polarized light). After normalization of the measured data, the average value was matched to the average value of the theoretical curve, but the reflectivity at the angle where SPP resonance occurs was too high in comparison to the calculated reflectivity.

By fitting a theoretical curve to the measured curve with the appropriate parameters, the complex refractive index of this aluminium sample was determined to a value of $\tilde{n}_{Al} = 1.409 + 9.9 \cdot i$ (at a wavelength of 1040 nm) and the thickness of the layer was 12.9 nm. The maximum propagation length of a SPP if only the Ohmic losses would have been taken into account is given in equation (2.9). With the dielectric constant of air assumed to be one (and thus the losses in air been neglected) and the dielectric constant of aluminium being calculated with use the relation $\epsilon = \tilde{n}^2$, the maximum propagation length of a SPP excited at this sample could be calculated to a maximum of 59 μm if only Ohmic losses are taken into account.

As noted before, the propagation length of a SPP is not only finite due to Ohmic losses in the metal, but also due to radiation back into the coupling medium. In order to give an indication of the maximum propagation length of the SPP due to coupling back into the prism the width of the dip in the angular reflectivity spectrum has been determined. If the dip in the angular reflectivity curve of a certain configuration is narrow, the coupling of an incoming wave to the SPP occurs at stricter conditions than in a configuration with a wide dip.

In the reverse process; radiation of the SPP to the coupling medium, a narrow dip corresponds to stricter conditions for coupling back into the coupling prism, making it 'harder' for the SPP to lose energy by radiating back into the coupling prism. The conclusion which can be drawn is that a wider dip in the angular reflectivity curve of a configuration indicates more energy losses due to radiation back to the coupling prism, causing a shorter propagation length (if only radiation losses back into the prism are taken into account) than a configuration with a narrower dip in the angular reflectivity curve [11].

In order to give an indication of the width of the dip in the angular reflectivity curve the following definition has been made (Figure 4.13)

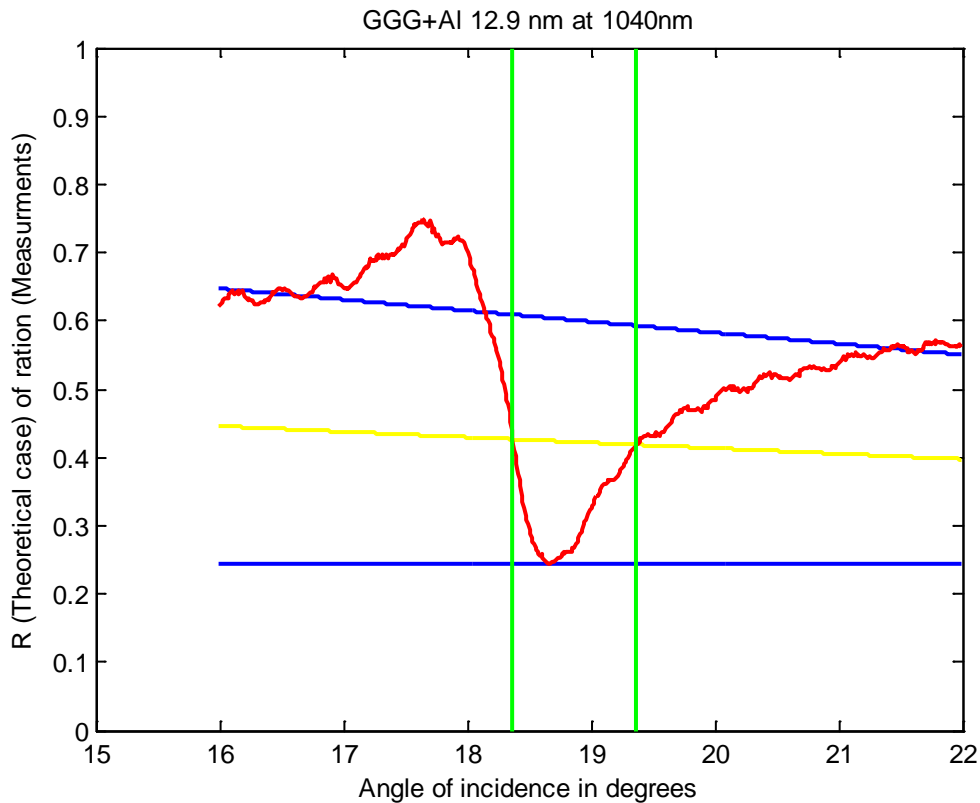


Figure 4.4: Definition of the width of the dip.

In Figure 4.13 the measured angular reflectivity spectrum of a 12.9 nm thick aluminium layer mounted on a GGG prism has been displayed in red. The blue lines are the asymptotic values of the reflectivity and the minimum reflectivity. The yellow line lies between the blue lines. At the angles where the angular reflectivity spectrum intersects the yellow line vertical green lines were drawn. The difference in the two angles of the green lines was defined as the width of the dip in the angular reflectivity spectrum. In this case the width of the angular reflectivity spectrum of a 12.9 nm thick layer of aluminium at 1040 nm wavelength was calculated to be 0.99 degrees.

In total 6 samples were measured at the two available wavelengths. This corresponds to 12 angular reflectivity spectra, displayed in Appendix D. Each angular reflectivity curve has been analysed in the way described above. The maximum propagation length with only Ohmic losses taken into account and the width in the dip in the angular reflectivity spectrum are summarized in Table 4.1.

Sample number	Metal	Wavelength=1040 nm			Wavelength=2330 nm		
		d (nm)	Prop. length due to Ohmic losses (μm)	Width of dip (degrees)	d (nm)	Prop. length due to Ohmic losses (μm)	Width of dip (degrees)
1.	Copper	30.9 \pm 4	44.5 \pm 22.4	0.74	70.0 \pm 10	91.2 \pm 21.8	0.52
2.	Copper	23.0 \pm 3	69.3 \pm 25.8	1.59	130.0 \pm 20	20.2 \pm 11.2	2.23
3.	Gold	36.4 \pm 4	96.0 \pm 17.2	0.32	44 \pm 5	198.7 \pm 25.5	0.47
4.	Gold	14.0 \pm 2	181.3 \pm 30.4	0.78	100.0 \pm 20	32.5 \pm 18.7	1.13
5.	Aluminium	12.9 \pm 2	59.0 \pm 32.8	0.99	Not determined		
6.	Aluminium	Not determined			23.0 \pm 3	148.5 \pm 20.2	0.72

Table 4.1: Determined thicknesses, maximum propagation lengths due to Ohmic losses and widths of the dip in the angular reflectivity spectrum for 6 samples measured at two wavelengths.

In Table 4.1 the thicknesses are determined by fitting the theoretical curve to the measured curve. The error in the thickness given in Table 4.1 has been estimated by changing the value of the thickness. If approximately 90 percent of the theoretical curve did not match the range of error in the measured curve, the error limit has been reached and the difference between this value and the optimal value was taken as the error.

The error in the calculated propagation lengths are in the range of 12 to 57 percent of the value of the propagation length. The calculated propagation lengths were dependent of the imaginary part and the real part of the dielectric constant of the metal (equation 2.9). A big change in the imaginary part (10%) however caused only a small change (approximately 2%) in the theoretical curve. A small error in the measured angular reflectivity spectrum caused a big error in the dielectric constant of the material and thus a big error (12 to 57 percent of the calculated value) in the calculated propagation length.

5 Discussion

In general, minima in the measured angular reflectivity spectra (Appendix D) were observed. In order to exclude an error in the measurements as an explanation of these dips, the errors involved with this experiment were estimated. As can be seen, errors in the recorded data cannot a structural dip in the angular reflectivity spectrum as deep as the observed dips.

The measured angle at which SPP resonance occurs (the dip) did fit the angle of resonance of the theoretical curve, the depth of the measured dip did however not match the depth of the theoretical dip, calculated with dielectric constants found in literature and thicknesses at which the layers has been deposited. A theoretical curve calculated with parameters to fit the data led to big deviations of these parameters relative to the values in literature. A big change in the parameters of the metal (10 percent of the value) caused a small change in the amplitude of the dip (less than 2 percent of the total depth). As a result, a small error in the amplitude of the dip in the angular reflectivity spectrum led to a big error in the parameters of the metal layer.

Errors of 12 up to 57 percent were determined in the calculated propagation lengths. The main reason for these high errors is that the propagation lengths were calculated with the parameters of the metal. A large error in (especially) the determined imaginary parts of the dielectric constants of the used metals led to large errors in the calculated propagation lengths. To illustrate this, these are compared with the imaginary part of the used materials found in literature (Table 5.1).

	Wavelength	Im(\tilde{n})	Im(\tilde{n})	
Metal	(nm)	measured	literature	Source
Copper	1040	5.8±0.5	6.9	[9]
Copper	2330	8±0.8	12.4	[9]
Copper	1040	6.7±0.7	6.9	[9]
Copper	2330	4.8±0.5	12.4	[9]
Gold	1040	6.9±0.5	7.1	[9]
Gold	2330	10.5±0.9	14.6	[9]
Gold	1040	8.5±0.7	7.1	[9]
Gold	2330	5.7±0.4	14.6	[9]
Aluminium	1040	9.9±0.5	9.9	[10]
Aluminium	2330	23.5±1.2	23.5	[10]
Aluminium	2330	13±0.8	23.5	[10]

Table 5.1: Measured and literature values of the imaginary parts of the refractive index.

As can be seen, the measured imaginary parts of the dielectric constants of the metals are only roughly comparable to the values in literature.

Besides the large error in the imaginary part of the dielectric constants of the used metals, large error were also observed in other parameters, such as the thickness of the metal films. The metal films are deposited onto the lithium niobate. For some layers the deposited thicknesses could be measured with a profilometer. The first column in Table 5.2 gives the thickness of the layer at which the deposition machine was set. The second column gives the thickness measured with a profilometer (if measuring this thickness was possible) and the third column gives the thickness determined with the angular reflectivity spectrum at 1040 nm and the fourth column gives the thickness of the film determined with the angular reflectivity spectrum at 2330 nm.

Sample number	Metal	deposited d (nm)	profilometer d (nm)	1440 nm d (nm)	2330 nm d (nm)
1.	Copper	34	30.92	30.9±4	70.0±10
2.	Copper	23	x	23.0±3	130.0±20
3.	Gold	30	36.42	36.4±4	44.0±5
4.	Gold	20	24.05	14.0±2	100.0±20
5.	Aluminium	13	x	12.9±2	x
6.	Aluminium	23	x	x	23.0±3

Table 5.2: Measured thicknesses of the layers.

As can be seen, the measured thicknesses with the use of the angular reflectivity spectrum deviate strongly from the measured thicknesses with the profilometer and are not the same at different wavelengths. This is assigned to the fact that determination of the thickness was based on the angular reflectivity spectrum, which might have had systematic errors due to normalisation, beam divergence or losses in intensity of the beam at different angles of incidence. All quantities which are dependent on the absolute value of reflectivity are less trustworthy (the thickness of the layer, the imaginary part of the refractive index and thus the propagation length if only Ohmic losses are taken into account) than quantities which are dependent on the general shape of the curve, such as the angle at which SPP resonance occurs.

6 Conclusion

The motivation of this research was to excite surface plasmon polaritons with a long propagation length (more than 100 μm). The goal of this experiment was to excite surface plasmon polaritons with a long propagation length via excitation with a near infrared and mid-infrared wavelength radiation.

The excitation of a SPP shows up at a certain angle in the angular reflectivity spectrum, as can be derived from the Fresnel equations and the dispersion relations of the SPP and the coupling medium. In our measurements, performed with near infrared light of a laser (1040 nm) and an optical parametric oscillator (2330 nm), dips in the angular reflectivity spectra of 6 different metal samples were observed. It can thus be concluded that we excited SPPs in the near- and mid-infrared wavelength range.

In Table 5.1 the measured propagation lengths if only Ohmic losses are taken into account were given. A 14 nm thick layer of gold at a wavelength of 1040 nm, a 40 nm thick layer of gold at 2330 nm and a 23 nm thick layer of aluminium at 2330 nm were measured to give a propagation length of more than 100 μm . These propagation lengths were a maximum value, and did only take account the Ohmic losses.

Further experiments have to be done in order to determine the propagation length of the excited SPP if also radiation and scattering are taken into account. Variations in thickness of the layer or the growth of the layer in so-called islands could have caused the radiation of the SPP to be high. The real propagation length of a SPP might, for example, be determined by use of an AFM.

An important improvement in future experiments would be the normalisation of the angular reflectivity spectrum. So far, in this experiment the process of fitting the theoretical curve with appropriate parameters to the measured curve, in combination with normalisation of the measured curve to the theoretical curve, has led to a big error in the determined thicknesses, imaginary part of the refractive indices and maximum propagation length due to Ohmic losses. Before each measurement the prism should be taken off the stage and the intensity of the beam should be measured with the photodetector. The ratio of the intensities is in that case equal to a reflectivity of one.

7 Appendices

7.1 Appendix A: Dispersion relation of a SPP

Electromagnetic waves in matter

In Paragraph 2.1 the properties of a SPP were discussed. A SPP is an electromagnetic wave which can thus be described with a classical wave equation derived from Maxwell's equations:

$$\nabla^2 \mathbf{E} = \frac{1}{v^2} \frac{\partial^2 \mathbf{E}}{\partial t^2} \quad (\text{A.1})$$

Where \mathbf{E} is the electric field and v is the speed of light in the medium ($v = c/n$).

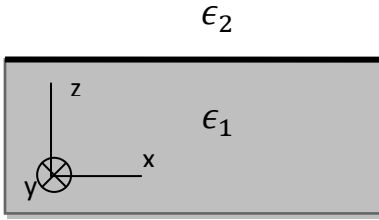


Figure A. 1: An interface of two media with dielectric constants ϵ_1 , ϵ_2 .

Defined are two layers of different materials, with dielectric constants ϵ_1 for $z < 0$ and ϵ_2 for $z > 0$ (see Figure A.1)

The wave equations have two different solutions, one for s-polarized waves and one for p-polarized waves. As can be shown, a SPP can only be a p-polarized beam, with the solution of equation A.1 in layer number j [2] :

$$\mathbf{E}_j = \begin{pmatrix} E_{j,x} \\ 0 \\ E_{j,z} \end{pmatrix} e^{ik_x - i\omega t} e^{ik_{j,z}z} \quad \text{for } j = 1, 2. \quad (\text{A.2})$$

Where $E_{j,x}$ and $E_{j,z}$ give the amplitude of the electromagnetic wave in the x- respectively z-direction. k_x and k_z are the wave vectors in the x and the z direction and ω is the frequency of the wave.

If (A.2) is substituted in (A.1) then the following must hold:

$$k_x^2 + k_{j,z}^2 = \epsilon_j k^2, \quad j = 1, 2. \quad (\text{A.3})$$

Where k is the total wave vector amplitude in vacuum, $k = \omega/c$. The displacement field in both half spaces has to be free of source charge, $\nabla \cdot \mathbf{D} = 0$ leads to

$$k_x E_{j,x} + k_{j,z} E_{j,z} = 0, \quad j = 1, 2. \quad (\text{A.4})$$

Solving (A.4) for $E_{j,x}$ and substitution this into (A.2) gives:

$$\mathbf{E}_j = E_{j,x} \begin{pmatrix} 1 \\ 0 \\ -k_x/k_{j,z} \end{pmatrix} e^{ik_x - i\omega t} e^{ik_{j,z}z} \quad j = 1, 2. \quad (\text{A.5})$$

Boundary conditions

On the interface between two materials boundary conditions must be taken into account. If there is no free charge or free current at the interface, then

$$\epsilon_1 \mathbf{E}_1^\perp = \epsilon_2 \mathbf{E}_2^\perp \quad (\text{A.6.1}) \quad \mathbf{E}_1^\parallel = \mathbf{E}_2^\parallel \quad (\text{A.6.2})$$

$$\mathbf{B}_1^\perp = \mathbf{B}_2^\perp \quad (\text{A.6.3}) \quad \frac{1}{\mu_1} \mathbf{B}_1^\parallel = \frac{1}{\mu_2} \mathbf{B}_2^\parallel \quad (\text{A.6.4})$$

Surface plasmon polariton solution

Combining equation (A.4) for $j=1,2$ with the boundary conditions (A.6.1) and (A.6.3) will form a 4×4 matrix. Setting the determinant of this matrix equal to zero leads to

$$\epsilon_1 k_{1,z} = \epsilon_2 k_{2,z} \quad (\text{A.7})$$

For the last step we combine (A.7), (A.3) for $j=1$ and $j=2$ and then solve for k_x , which leads to a dispersion relation between the wave vector along the direction of propagation of the SPP and the angular frequency ω .

$$k_x^2 = \left(\frac{\epsilon_1 \epsilon_2}{\epsilon_1 + \epsilon_2} \right) \frac{\omega^2}{c^2} \quad (\text{A.8})$$

If the last three equations are solved for $k_{j,z}$ instead of k_x , the following expression will appear

$$k_{j,z}^2 = \left(\frac{\epsilon_j^2}{\epsilon_1 + \epsilon_2} \right) \frac{\omega^2}{c^2} \quad (\text{A.9})$$

This is the wave vector of the SPP which is perpendicular to the interface in the j^{th} layer.

$$k_{x,SPP}^2 = \left(\frac{\epsilon_1 \epsilon_2}{\epsilon_1 + \epsilon_2} \right) \frac{\omega_{SPP}^2}{c^2} \quad (\text{A.10})$$

$$k_{z,SPP}^2 = \left(\frac{\epsilon_1^2}{\epsilon_1 + \epsilon_2} \right) \frac{\omega_{SPP}^2}{c^2} \quad z > 0 \quad (\text{A.11})$$

$$k_{z,SPP}^2 = \left(\frac{\epsilon_2^2}{\epsilon_1 + \epsilon_2} \right) \frac{\omega_{SPP}^2}{c^2} \quad z < 0 \quad (\text{A.12})$$

Analyses of s-polarized waves [8]

For $z > 0$ we can write for the electric and magnetic field:

$$\mathbf{E}_2 = (0, E_{2,y}, 0) e^{ik_x x - k_{2,z} z - i\omega t} \quad (\text{A.13})$$

$$\mathbf{H}_2 = \frac{E_{2,y} c}{i\omega} (k_{2,z}, 0, ik_x) e^{ik_x x - k_{2,z} z - i\omega t} \quad (\text{A.14})$$

Referring to Figure (A.1) for the interface orientation. For $z < 0$ the electric and magnetic fields are:

$$\mathbf{E}_1 = (0, E_{1,y}, 0) e^{ik_x x - k_{1,z} z - i\omega t} \quad (\text{A.15})$$

$$\mathbf{H}_1 = \frac{E_{1,y}c}{i\omega} (-k_{1,z}, 0, ik_x) e^{ik_x x - k_{1,z} z - i\omega t} \quad (\text{A.16})$$

The continuity of the tangential components of the electric and magnetic fields across the interface at $z=0$ yields the pair of equations:

$$E_{1,y} = E_{2,y}, \quad E_{2,y} \frac{c}{i\omega} k_{2,z} = -E_{1,y} \frac{c}{i\omega} k_{1,z} \quad (\text{A.17})$$

which can be combined into the single equation:

$$(k_{1,z} + k_{2,z})E_{2,z} = 0 \quad (\text{A.18})$$

Both k_z vectors are positive, because we have in both media decaying waves away from the interface. Then $E_{2,z}$ must be 0, then $E_{1,z}$ also is equal to 0. Concluded must be that s-polarized surface plasmon polaritons cannot exist.

7.2 Appendix B: Drude model

In section 2.1 the wave vector solution was modelled with the Drude model. The basic optical properties of a metal can be modelled in the approximation of a plasma model, in which a gas of free electrons is moving in an immobile background of ion cores. Lattice potential and electron-electron interactions are not taken into account.

The electrons oscillate in response to an applied electromagnetic field and the motion of the electrons is damped via collision occurring at a characteristic collision frequency $\gamma=1/\tau$. τ is the relaxation time of the free electron gas.

The equation of motion of an electron in the plasma subject to an electric field is:

$$m\ddot{\mathbf{x}} + m\gamma\dot{\mathbf{x}} = -e\mathbf{E}, \quad (\text{B.1})$$

where m is the mass of an electron, \mathbf{x} is the displacement, e is the charge of an electron and \mathbf{E} is the applied electric field.

We assume a harmonic time dependence $\mathbf{E}(t) = \mathbf{E}_0 e^{-i\omega t}$ with frequency ω of the driving field. The response of the electrons to this applied field is:

$$\mathbf{x}(t) = \frac{e}{m(\omega^2 + i\gamma\omega)} \mathbf{E}(t) \quad (\text{B.2})$$

The displacement contributes to a polarization $\mathbf{P} = -n \cdot e \cdot \mathbf{x}$, with n the number of electrons per unit volume:

$$\mathbf{P} = -\frac{ne^2}{m(\omega^2 + i\gamma\omega)} \mathbf{E} \quad (\text{B.3})$$

Inserting (B.3) into $\mathbf{D} = \epsilon_0 \mathbf{E} + \mathbf{P}$ the displacement field can then be written as:

$$\mathbf{D} = \epsilon_0 \left(1 - \frac{\omega_p^2}{\omega^2 + i\gamma\omega} \right) \mathbf{E}, \quad (\text{B.4})$$

where $\omega_p^2 = ne^2/\epsilon_0 m$ is the plasma frequency of the free electron gas. \mathbf{D} is also equal to $\mathbf{D} = \epsilon_0 \epsilon \mathbf{E}$. From (B.4) the dielectric constant is given by [1]:

$$\epsilon(\omega) = 1 - \frac{\omega_p^2}{\omega^2 + i\gamma\omega} \quad (\text{B.5})$$

The real and the imaginary components are:

$$\Re(\epsilon(\omega)) = 1 - \frac{\omega_p^2 \tau^2}{1 + \omega^2 \tau^2} \quad (\text{B.6})$$

$$\Im(\epsilon(\omega)) = \frac{\omega_p^2 \tau}{\omega(1 + \omega^2 \tau^2)} \quad (\text{B.7})$$

7.3 Appendix C: Fresnel's equations [4]

Throughout the text there were theoretical red and green coloured curves plotted with the purpose for comparing them with the measured curves and extract parameters from them. The calculation of these theoretical curves is based on Fresnel's equations which will be derived next.

Suppose there is a system of N layers described by the (complex) refractive indices $\tilde{n}_1, \tilde{n}_2, \tilde{n}_3, \dots, \tilde{n}_N$ where $\tilde{n}_j = n_j + i \cdot \kappa_j$ and the relation between an incoming wave and a reflected wave is needed.

The Fresnel's coefficients give the amplitudes of the reflected (r) and the transmitted light (t). If we consider an incoming wave in medium j and the transmitted light in medium k for a two layered system:

For s-polarized waves:

$$r_{j,k}^s = \frac{\tilde{n}_j \cdot \cos(\theta_j) - \tilde{n}_k \cdot \cos(\theta_k)}{\tilde{n}_j \cdot \cos(\theta_j) + \tilde{n}_k \cdot \cos(\theta_k)} \quad \text{C.1}$$

$$t_{j,k}^s = \frac{2 \cdot \tilde{n}_j \cdot \cos(\theta_j)}{\tilde{n}_j \cdot \cos(\theta_j) + \tilde{n}_k \cdot \cos(\theta_k)} \quad \text{C.2}$$

And for p-polarized waves:

$$r_{j,k}^p = \frac{\tilde{n}_k \cdot \cos(\theta_j) - \tilde{n}_j \cdot \cos(\theta_k)}{\tilde{n}_k \cdot \cos(\theta_j) + \tilde{n}_j \cdot \cos(\theta_k)} \quad \text{C.3}$$

$$t_{j,k}^p = \frac{2 \cdot \tilde{n}_j \cdot \cos(\theta_j)}{\tilde{n}_k \cdot \cos(\theta_j) + \tilde{n}_j \cdot \cos(\theta_k)} \quad \text{C.4}$$

where θ_j is the angle of the incoming wave to the normal of the interface. θ_k is the angle of the transmitted light to the normal of the interface. If the refractive indices and θ_j are known, θ_k can be calculated using Snell's law.

The situation considered so far was the case of two layers and one interface. In the case of multiple layers the total reflected wave is the sum of all the reflections in the middle layers, that is, the layers that are between the first and the last layer. To illustrate this we consider a system containing one layer sandwiched between two other layers (see Figure C.1)

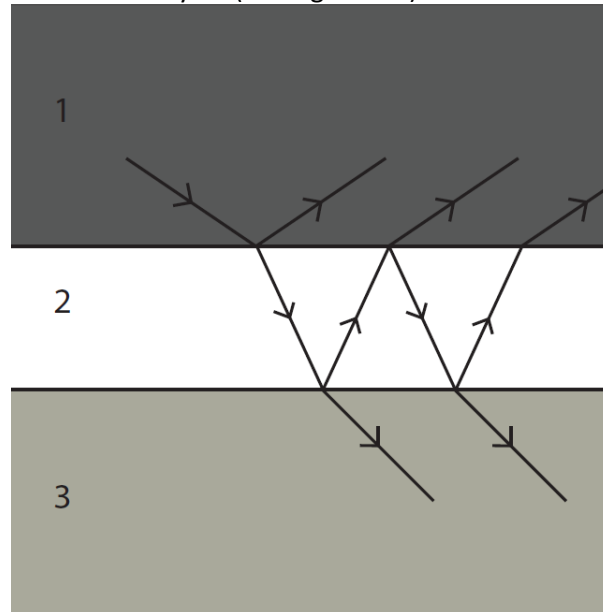


Figure C. 1: A three layered system of three different dielectric materials.

In this case the reflected light wave at the surface between media 2 and 3 gets reflected again and again, and the total reflected light will have an amplitude:

$$r = r_{1,2} + t_{1,2} \cdot r_{2,3} \cdot t_{2,1} + t_{1,2} \cdot r_{2,3}^2 \cdot r_{2,1} \cdot t_{2,1} + t_{1,2} \cdot r_{2,3}^3 \cdot r_{2,1} \cdot r_{2,1} \cdot t_{2,1} + \dots \quad \text{C.5}$$

Or, more compactly:

$$r = r_{1,2} + t_{1,2} \cdot t_{2,1} \cdot x \quad \text{C.6}$$

$$x \equiv r_{2,3} + r_{2,3}^2 \cdot r_{2,1} + r_{2,3}^3 \cdot r_{2,1}^2 + \dots \quad \text{C.7}$$

Equation C.7 can be written as an infinite series:

$$x \equiv r_{2,3} \cdot (1 + r_{2,1} \cdot r_{2,3} \cdot (\dots \quad \text{C.8}$$

Or

$$x \equiv r_{2,3} \cdot (1 + r_{2,1} \cdot x) \quad \text{C.9}$$

Especially in the case of thin layers, compared to the coherence length of the incident light, the phase differences of the different reflected waves have also to be taken into account.

A wave travelling back and forth in layer number j gets an extra phase $2 \cdot \delta_j$ where

$$\delta_j = \frac{2 \cdot \pi \cdot d_j \cdot \tilde{n}_j \cdot \cos(\theta_j)}{\lambda} \quad \text{C.10}$$

So the constant x should be redefined to:

$$x \equiv e^{2 \cdot i \cdot \delta_2} \cdot r_{2,3} \cdot (1 + r_{2,1} \cdot x) \quad \text{C.11}$$

$$x = \frac{e^{2 \cdot i \cdot \delta_2} \cdot r_{2,3}}{1 - e^{2 \cdot i \cdot \delta_2} \cdot r_{2,3} \cdot r_{2,1}} \quad \text{C.12}$$

Notice that, if the thickness of a layer n is zero, then also $\delta_n = 0$ and x can be written as equation C.9.

Using the relations:

$$r_{2,1} = -r_{1,2} \quad \text{C.13}$$

$$t_{2,1} \cdot t_{1,2} + r_{2,1} \cdot r_{2,1} = 1 \quad \text{C.14}$$

And combining these with equations C.12, equation C.6 can be written as:

$$r = r_{1,2} + t_{1,2} \cdot t_{2,1} \cdot x \quad \text{C.15}$$

$$r = r_{1,2} + t_{1,2} \cdot t_{2,1} \cdot \frac{e^{2 \cdot i \cdot \delta_2} \cdot r_{2,3}}{1 - e^{2 \cdot i \cdot \delta_2} \cdot r_{2,3} \cdot r_{2,1}} \quad \text{C.16}$$

$$r = \frac{r_{1,2} + e^{2 \cdot i \cdot \delta_2} \cdot r_{2,3}}{1 + e^{2 \cdot i \cdot \delta_2} \cdot r_{2,3} \cdot r_{2,1}} \quad \text{C.17}$$

In the same way, the amplitude of the transmitted wave (t) can be written as:

$$t = t_{1,2} \cdot t_{2,3} \cdot y \quad \text{C.18}$$

$$y = \frac{e^{2 \cdot i \cdot \delta_2}}{1 - e^{2 \cdot i \cdot \delta_2} \cdot r_{2,3} \cdot r_{2,1}} \quad \text{C.19}$$

$$t = \frac{e^{2 \cdot i \cdot \delta_2} \cdot t_{1,2} \cdot t_{2,3}}{1 + e^{2 \cdot i \cdot \delta_2} \cdot r_{1,2} \cdot r_{2,3}} \quad \text{C.20}$$

Equations C.17 and C.20 give the reflectivity resp. Transmittance of one layer sandwiched between two other layers.

When considering multiple layers, it is useful to make some definitions, shown in Figure C.2;

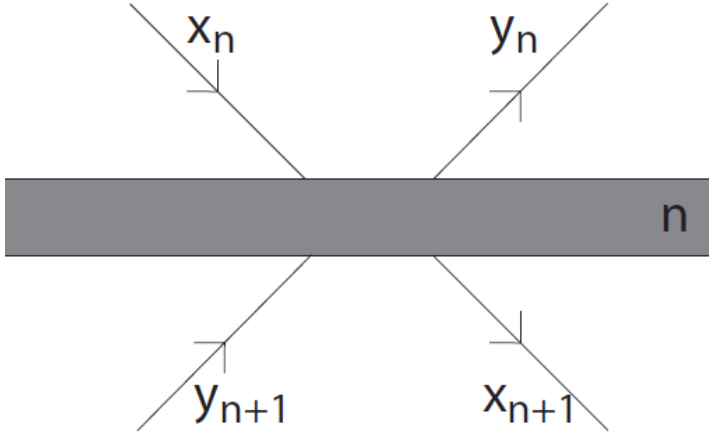


Figure C. 2: Schematic view of layer number n.

x_n is the amplitude of the transmitted wave of the layer n-1, y_{n+1} is the amplitude of the reflected light from layer n+1, y_n and x_{n+1} are the amplitudes of the reflected resp. transmitted light of layer n.

The amplitudes are related in the following way:

$$\begin{bmatrix} x_n \\ y_n \end{bmatrix} = \frac{1}{t_{n-1,n}} \cdot \begin{bmatrix} 1 & r_{n-1,n} \\ r_{n-1,n} & 1 \end{bmatrix} \cdot \begin{bmatrix} e^{-i \cdot \delta_n} & 0 \\ 0 & e^{i \cdot \delta_n} \end{bmatrix} \cdot \begin{bmatrix} x_{n+1} \\ y_{n+1} \end{bmatrix} \quad \text{C.21}$$

Or, defining M_n :

$$\begin{bmatrix} x_n \\ y_n \end{bmatrix} = M_n \cdot \begin{bmatrix} x_{n+1} \\ y_{n+1} \end{bmatrix} \quad \text{C.22}$$

$$M_n \equiv \frac{1}{t_{n-1,n}} \cdot \begin{bmatrix} 1 & r_{n-1,n} \\ r_{n-1,n} & 1 \end{bmatrix} \cdot \begin{bmatrix} e^{-i \cdot \delta_n} & 0 \\ 0 & e^{i \cdot \delta_n} \end{bmatrix} \quad \text{C.23}$$

This formula gives the relation between the four waves given in Figure C.2. The parameters needed are the Fresnel's coefficients (equations C.1-4) and the phase shift in this layer (equation C.10).

If there are N layers, and thus N+1 interfaces, the reflectivity of the whole system can be calculated by multiplying all the matrices of each layer (C.21):

$$\begin{bmatrix} x_1 \\ y_1 \end{bmatrix} = M_1 \cdot M_2 \cdot M_3 \cdot M_4 \cdot \dots \cdot M_{N-1} \cdot M_N \cdot M_{N+1} \cdot \begin{bmatrix} x_{N+1} \\ y_{N+1} \end{bmatrix} \quad \text{C.24}$$

$$\begin{bmatrix} x_1 \\ y_1 \end{bmatrix} = M_T \cdot \begin{bmatrix} x_{N+1} \\ y_{N+1} \end{bmatrix} \quad \text{C.25}$$

with

$$M_T = \begin{bmatrix} M_{T1,1} & M_{T1,2} \\ M_{T2,1} & M_{T2,2} \end{bmatrix} \equiv M_1 \cdot M_2 \cdot \dots \cdot M_N \cdot M_{N+1} \quad \text{C.26}$$

Setting y_{N+1} to zero makes it possible to calculate the ratio of amplitude between the incoming wave and the reflected wave. $y_{N+1} = 0$ leads to

$$x_1 = M_{T1,1} \cdot x_{N+1} \quad \text{C.27}$$

$$y_1 = M_{T2,1} \cdot x_{N+1} \quad \text{C.28}$$

The ratio between an incoming wave (x_n) and the reflected wave (y_1) is given by

$$\frac{x_1}{y_1} = \frac{M_{T1,1}}{M_{T2,1}} \quad \text{C.29}$$

Which gives a direct relation between the parameters of the system and the reflectivity (R):

$$R = \left(\frac{M_{T1,1}}{M_{T2,1}} \right)^2 \quad \text{C.29}$$

7.4 Appendix D: Angular reflectivity spectra of the samples

In Figures D.1 to D.11 the measured angular reflectivity spectra were plotted in blue at a range of angles around the angle of SPP resonance. In red are the theoretical curves plotted which fitted the experimental results the best. In yellow were plotted the maximum and minimum value of the reflectivity taking into account the maximum errors in the measurements.

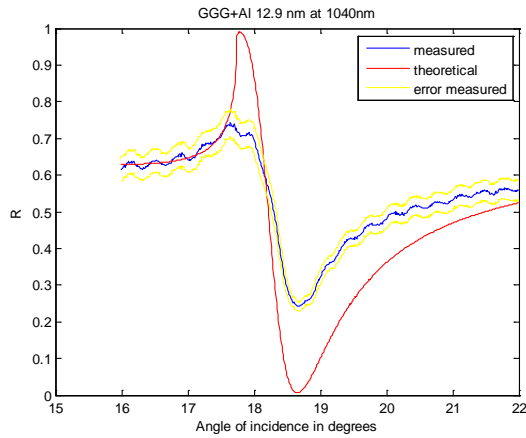


Figure D. 1: Angular reflectivity spectrum measured for GGG + Al 12.9 nm at 1040 nm

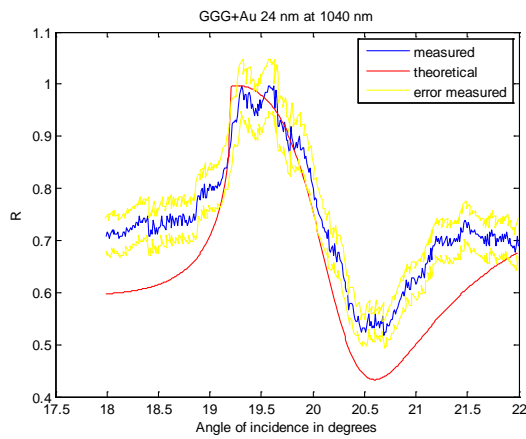


Figure D. 2: Angular reflectivity spectrum measured for GGG + Au 24 nm at 1040 nm

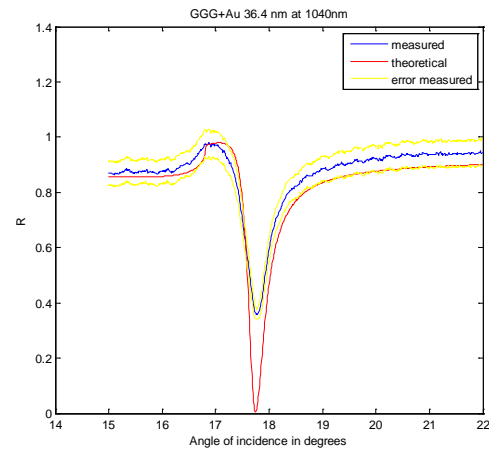


Figure D. 3: Angular reflectivity spectrum measured for GGG + Au 36.4 nm at 1040 nm

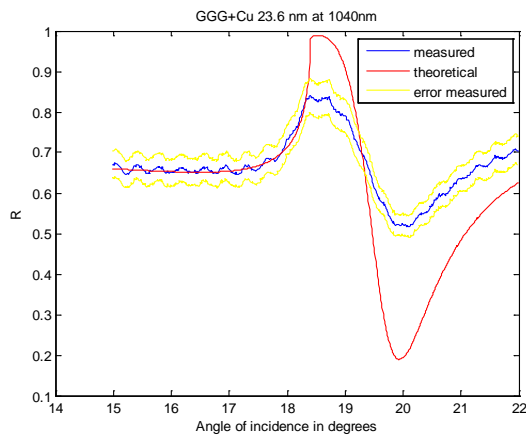


Figure D. 4: Angular reflectivity spectrum measured for GGG + Cu 23.6 nm at 1040 nm

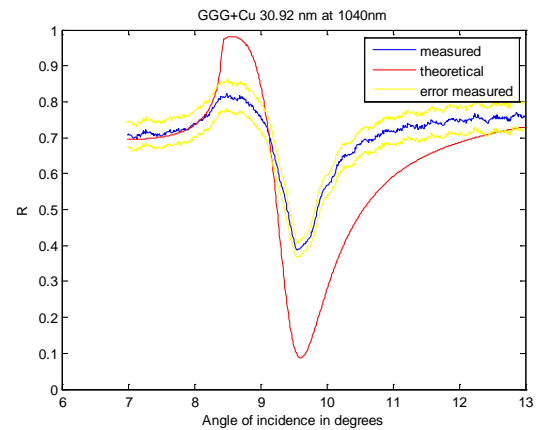


Figure D. 5: Angular reflectivity spectrum measured for GGG + Cu 30.92 nm at 1040 nm

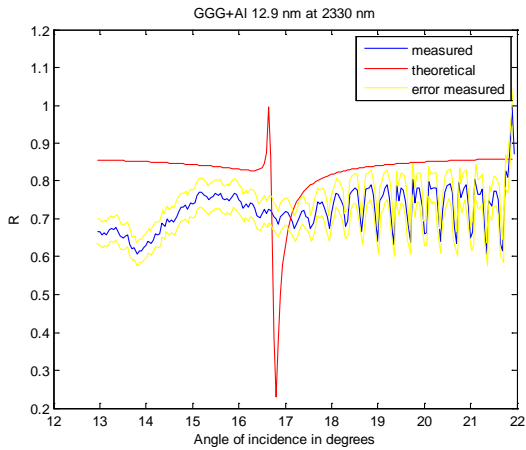


Figure D. 6: Angular reflectivity spectrum measured for GGG + Al 12.9 nm at 2330 nm

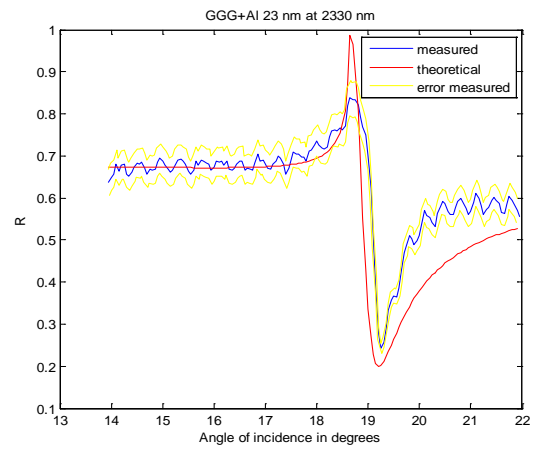


Figure D. 7: Angular reflectivity spectrum measured for GGG + Al 23 nm at 2330 nm

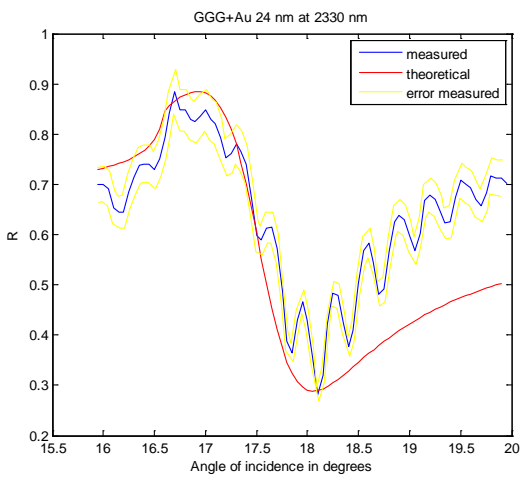


Figure D. 8: Angular reflectivity spectrum measured for GGG + Au 24 nm at 2330 nm

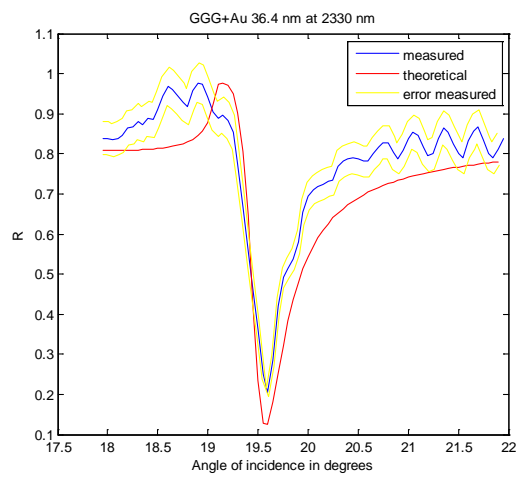


Figure D. 9: Angular reflectivity spectrum measured for GGG + Au 36.4 nm at 2330 nm

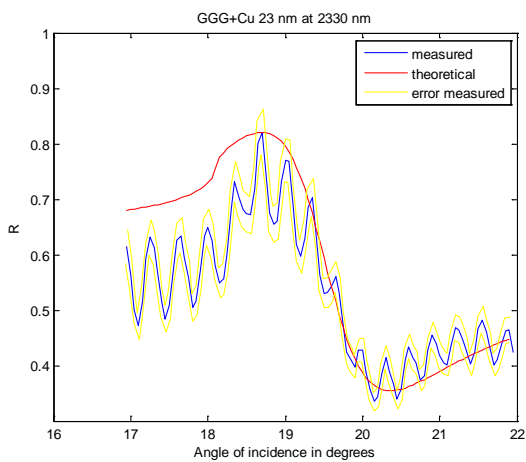


Figure D. 10: Angular reflectivity spectrum measured for GGG + Cu 23.6 nm at 2330 nm

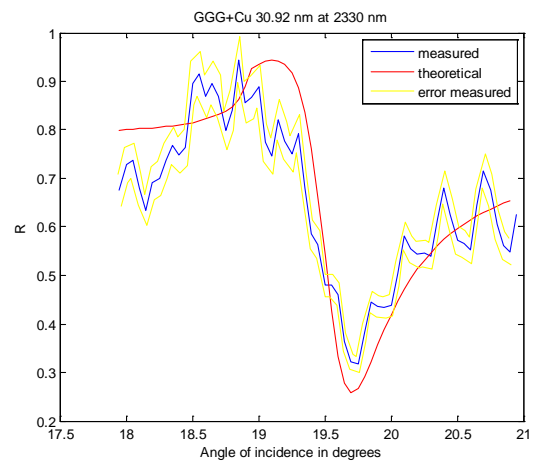


Figure D. 11: Angular reflectivity spectrum measured for GGG + Cu 30.92 nm at 2330 nm

The error in the angle of incidence was estimated to be about 0.05 degrees, which was five times the typical size of the step in angle used to measure the curve. The error in the reflectivity was dependent on the shape of the power profile of the beam and the specifications of the photodetector. The error in the reflectivity of the system was set at 5 percent of the measured reflectivity.

7.5 Appendix E: Measured thicknesses with a profilometer

The deposition technique used to make the thin films cannot make the layers precisely the thickness wanted. Errors of 6 nm are not rare and therefore the thicknesses of the layers were measured with a profilometer. With a knife a scratch was made in the sample. In figures E.1 to E.3, the measured profiles were displayed for 3 layers. The profiles of the other 3 layers show too much noise, and the thickness of these layers were therefore not determinable.

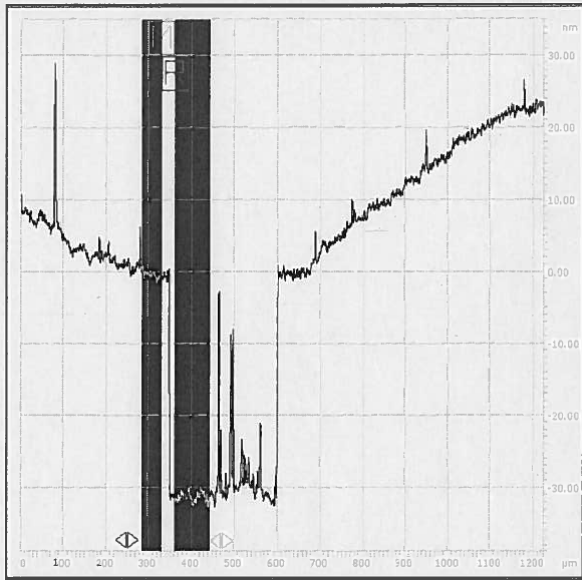


Figure E.1: The profile of a 33.6 nm thick copper layer. The measured thickness with the profilometer was 30.92 nm.

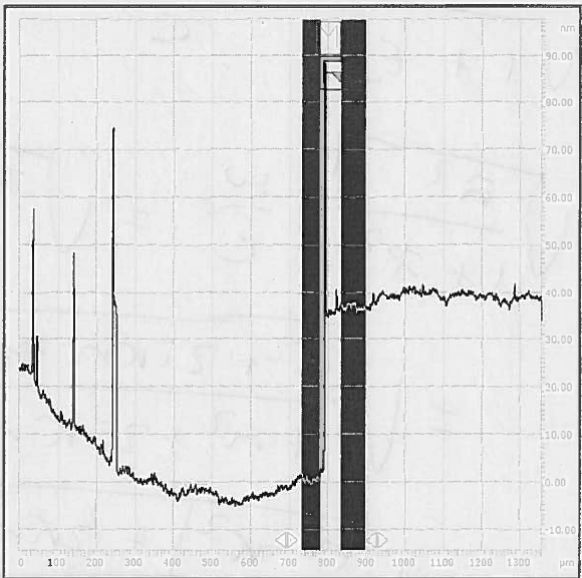


Figure E.2: The profile of a 30.0 nm thick gold layer. The measured thickness with the profilometer was 36.42 nm.

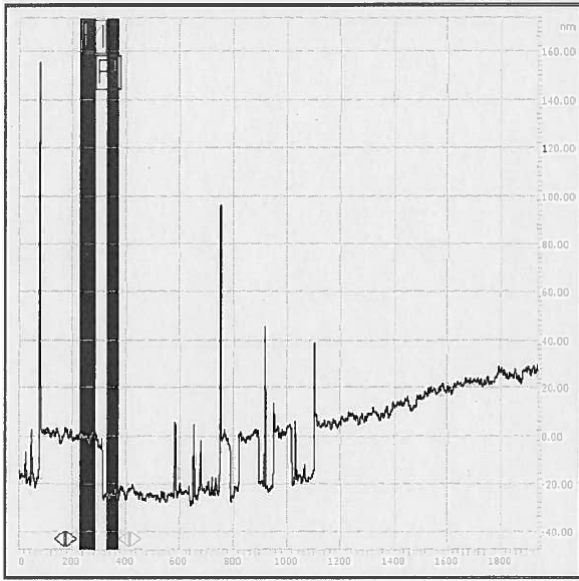


Figure E.3: The profile of a 20.2 nm thick gold layer. The measured thickness with the profilometer was 24.05 nm.

8 Bibliography

1. S. Wang, S. Boussaad and N.J. Tao, Surface plasmon resonance enhanced optical absorption spectroscopy for studying molecular adsorbates, *Review of Scientific Instruments*, 2001, Vol. 72, p. 3055.
2. B. Liedberg and C. Nylander and I. Lunstrom, Surface plasmon resonance for gas detection and biosensing, *Sensors and Actuators*, 1983, Vol. 4, pp. 299-304.
3. Stefan A. Maier, *Plasmonics: Fundamentals and applications*, 1st ed, Springer, New York, 2007
4. A. E. Craig, G. A. Olson and G. Sarid, Experimental observation of the long-range surface-plasmon polariton, *Optics letters*, 1983, Vol. 8, Iss 7, pp. 380-382.
5. E. Kretschmann, Die bestimmung optischer konstanten von metallen durch anregung von oberflächenplasmaschwingungen, *Zeitschrift für Physik A Hadrons and Nuclei*, 1971, Vol. 241, Iss. 4, pp. 313-324.
6. W.L. Barnes, A. Dereux and T. W. Ebbesen, Surface plasmon subwavelength optics, *Nature*, 2003, Vol. 424, Issue 6950, pp. 824-830.
7. D. L. Wood and K. Nassau, Optical properties of gadolinium gallium garnet, *Appl. Opt.* 25, Vol. 25, 1990, Issue 25, pp. 3704-3707.
8. E.D. Palik, *Handbook of Optical Constants of Solids*, Academic Press, Boston (1985)
9. *Microscope Objectives: Immersion media*, by Mortimer Abramowitz and Michael W. Davidson, *Olympus Microscopy Resource Center* (website), 2002.
10. A.D. Rakić, Algorithm for the determination of intrinsic optical constants of metal films: application to aluminum, *Applied optics* vol 34 number 22 pages 4755-4767 (1995)
11. Personal discussion with William Barnes
12. L. Novotny and B. Hecht, *Principles of nano-optics*, 1st ed, Cambridge Univ Pr, 2006
13. <http://www.ifm.liu.se/courses/TFYY67/Lect13.pdf>
14. Aleksandar D. Rakić. Algorithm for the determination of intrinsic optical constants of metal films: application to aluminium, *Appl. Opt.* 34, 4755-4767 (1995) doi:10.1364/AO.34.004755